

Phase Space Crystal Vibrations: Chiral Edge States with Preserved Time-reversal Symmetry

Lingzhen Guo,¹ Vittorio Peano,¹ and Florian Marquardt^{1,2}

¹Max Planck Institute for the Science of Light, Staudtstrasse 2, 91058 Erlangen, Germany

²Physics Department, University of Erlangen-Nuremberg, Staudtstrasse 5, 91058 Erlangen, Germany

(Dated: May 24, 2022)

It was recently discovered that atoms subject to a time-periodic drive can give rise to a crystal structure in phase space. In this work, we point out the atom-atom interactions give rise to collective phonon excitations of phase-space crystal via a pairing interaction with intrinsically complex phases that can lead to a phonon Chern insulator, accompanied by topologically robust chiral transport along the edge of the phase-space crystal. This topological phase is realized even in scenarios where the time-reversal transformation is a symmetry, which is surprising because the breaking of time-reversal symmetry is a strict precondition for topological chiral transport in the standard setting of real-space crystals. Our work has also important implications for the dynamics of 2D charged particles in a strong magnetic field.

Introduction.— The Quantum Hall current in a 2D electron gas pierced by a magnetic flux is insensitive to weak disorder, because it is carried by chiral edge states that do not have a counter-propagating counterpart [1, 2]. With the proposal of the Quantum Anomalous Hall Effect (QAHE) [3], Haldane showed that the key ingredient to engineer chiral edge states is not a net magnetic field flux, but rather the breaking of the time-reversal symmetry (TRS) itself. This insight has opened the way to the current focus on topological transport of neutral excitations such as photons [4–6], magnons [7, 8], phonons [9, 10] and cold atoms [11, 12].

In this work, we introduce a conceptually different way to generate robust chiral phonon transport, without requiring a breaking of the TRS. A *single quantum* particle moving on a closed path in phase space acquires a Berry phase [13–16]. Therefore, when one considers the quantum motion in an extended periodic phase-space potential, the resulting matter wave bandstructure supports non-trivial Chern numbers [15, 17, 18]. However, so far it was unclear how this could lead to the most important consequence of such Chern numbers, namely chiral edge channels, since it is not straightforward to produce a boundary of such a phase-space potential. Here we consider a different scenario, demonstrating a new mechanism that occurs already in the *classical* domain, but only if one considers an *interacting many-particle* system. When the particles arrange themselves in the extrema of the underlying phase-space potential, it gives rise to a so-called phase space crystal [15]. We will show that the phase-space crystal vibrations acquire a topologically non-trivial band structure, due to the combination of interactions and symplectic phase-space geometry. In contrast to the single-particle case, the boundary of the finitely extended phase space crystal naturally supports chiral edge channels in phase space, which are now of phononic (collective) nature. We show that these chiral edge channels can arise even when the driving preserves the time-reversal symmetry. Finally, we explore the im-

plications of our work for the crystal phase of 2D charged particles confined in the Lowest Landau Level (LLL) in the presence of a strong magnetic field.

Similar to Floquet approaches for topology [19, 20], we will be employing time-dependent driving, but in our case the drive itself need not break TRS to generate chiral transport, as a consequence of the nonlocal nature of the time reversal operation in phase space. Our construction produces topological channels in a 2D phase space, starting from 1D real space. This is reminiscent of synthetic dimensions [21–23], but unlike that concept, no extra controlled degree of freedom is needed, we automatically get chiral motion, and besides in synthetic dimensions it is very challenging to create non-trivial lattice structures [24] or local and isotropic interactions [22], in contrast to the present approach.

Model.— Consider cold atoms trapped in a quasi-1D elongated harmonic potential with the axial trapping frequency ω_{ax} and transverse trapping frequency $\omega_{tr} \gg \omega_{ax}$. The atoms are driven stroboscopically by multiple optical lattices with kicking frequency ω_{ax}/τ , where τ is the dimensionless kicking period. We sketch our model and the experimental implementation in Fig. 1(a)-(b). The single-atom Hamiltonian is given by

$$H_s = \frac{1}{2}(x^2 + p^2) + \sum_{n \in \mathbb{Z}} \sum_q K_q \cos(k_q x - \phi_q) \delta\left(\frac{t}{\tau} - \theta_q - n\right).$$

Here, we have rescaled the coordinate, momentum, time and energy by k^{-1} , $m\omega_{ax}/k$, ω_{ax}^{-1} and $m\omega_{ax}^2/k^2$, respectively, where m is the mass and k is the typical wave vector of the stroboscopic lattices.

For weak near-resonant driving ($|K_q| \ll 1$, $\tau/2\pi \approx 1$), the single-particle dynamics is dominated by fast harmonic oscillations with slowly changing quadratures (X, P) : $x = P \sin(2\pi t/\tau) + X \cos(2\pi t/\tau)$. Within the rotating-wave approximation this leads to a time-independent Hamiltonian $H_s(X, P)$ whose extrema represent stable points. By appropriately choosing parameters, they will form a lattice in phase space, e.g., the

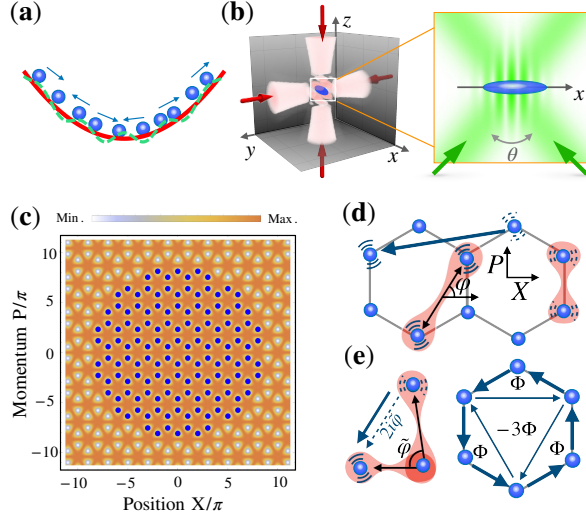


FIG. 1. (a) Sketch of our model: particles (blue) confined in a static harmonic potential (red) and driven by stroboscopic lattices (green). (b) Experimental implementation of our model with a cloud of cold atoms (blue) confined in quasi-1D tubes by two orthogonally polarized lasers (pink) and subject to a tuneable stroboscopic lattice formed by two lasers (green) intersecting at angle θ . (c) Density plot of single-particle Hamiltonian $H_s(X, P)$, with X, P in a rotating frame. The honeycomb lattice sites are occupied by atoms (blue), forming a disk-shaped crystal in phase space. (d) Sketch of coupling between the atoms' vibrations. The arrow indicates hopping of a vibrational excitation. The pink dumbbell-like shapes indicate pairwise creation (annihilation) of excitations. (e) Sketch of the pairing-interaction-induced hopping (left panel) and the resulting effective magnetic field (right panel). The induced non-reciprocal hopping pathway (dashed arrow) interferes with a direct hopping pathway (solid arrow), leading to a weak staggered magnetic flux of order $\sim \gamma/\omega_0$, see [25].

kicked harmonic oscillator [26–31]. Our model allows for more flexibility in the design of $H_s(X, P)$ and, thus, to realize any arbitrary phase space lattice [25]. For concreteness, in the remainder of the paper, we focus on a scenario where $H_s(X, P)$ supports a honeycomb lattice of stable points and is TRS invariant, $H_s(X, P) = H_s(X, -P)$. By superposing twelve equally spaced kicks [25], we have

$$H_s(\mathbf{Z}) = \frac{1}{2}\delta\omega|\mathbf{Z}|^2 - \frac{16}{9}\omega_0 \prod_{n=1}^3 \sin^2\left(\frac{1}{2}\mathbf{v}_n \cdot \mathbf{Z}\right). \quad (1)$$

Here, we have defined the vector $\mathbf{Z} \equiv (X, P)$, the detuning $\delta\omega \equiv 1 - 2\pi/\tau$, and three ancillary vectors $\mathbf{v}_1 = (1, \frac{1}{\sqrt{3}})$, $\mathbf{v}_2 = (-1, \frac{1}{\sqrt{3}})$, $\mathbf{v}_3 = (0, -\frac{2}{\sqrt{3}})$. For $\delta\omega = 0$, the minima of $H_s(\mathbf{Z})$ form a honeycomb lattice, cf. Fig. 1(c). The frequency of small vibrations about these stable points is $\omega_0 \propto |K_q|$ [25]. We note that $[X, P] = i\lambda$ with the effective Planck constant $\lambda = \hbar k^2/m\omega_{ax}$ (twice the square of the Lamb-Dicke parameter).

Many-body dynamics.— The interaction of neutral cold atoms in a tight 1D-trap is captured by an effective two-

body contact potential, $V(x_i - x_j) = \gamma\delta(x_i - x_j)$ [32]. Since atoms that are localized about distant phase-space points will still collide in the course of their lab-frame trajectories, the lab-frame contact interaction gives rise to an effective long-range interaction in the rotating frame [15, 33–36]. For $\lambda \ll 1$, the interaction is Coloumb-like [15, 35], $U(\mathbf{Z}_i - \mathbf{Z}_j) = \gamma\pi^{-1}|\mathbf{Z}_i - \mathbf{Z}_j|^{-1}$. Thus, we arrive at the many-body Hamiltonian

$$H = \sum_i H_s(\mathbf{Z}_i) + \frac{\gamma}{\pi} \sum_{i < j} \frac{1}{|\mathbf{Z}_i - \mathbf{Z}_j|}. \quad (2)$$

By introducing the *phase space force* $\mathbf{F}_i \equiv -\nabla_i H$ with $\nabla_i \equiv (\partial/\partial X_i, \partial/\partial P_i)$ and the unit direction vector $\hat{\mathbf{n}}$ perpendicular to the phase space plane, we can rewrite Hamilton's canonical equations as $\frac{d}{dt}\mathbf{Z}_i = \hat{\mathbf{n}} \times \mathbf{F}_i$, which is similar to the Lorentz force.

In the presence of dissipation, the stable points become attractors [37]. In other words, a non-interacting atom tends to relax towards the closest stable point. Introducing a sufficiently strong repulsive interaction ($\gamma > 0$) and initially preparing the atoms close to the origin will, thus, give rise to a disk-shaped crystal, see Fig. 1(b). We note that the atom-atom interaction tends to distort the equilibrium configuration. However, it is possible to strongly reduce this effect by counterbalancing the interaction-induced mean-field potential with a laser-generated potential. In practice, this can be achieved simply by choosing the appropriate detuning $\delta\omega$ instead of resonant driving [25], cf. Fig. 3(c).

Lattice dynamics.— Each atom oscillates around its equilibrium position, i.e., $\mathbf{Z}_L(t) = \mathbf{Z}_L^0 + \mathbf{u}_L(t)$ where $\mathbf{u}_L = (u_L^X, u_L^P)$ is the displacement on the lattice site L . The equilibrium points are determined by $\partial H/\partial u_L^\alpha = 0$ ($\alpha \in \{X, P\}$). By expanding the Hamiltonian Eq. (2) up to second order, we rewrite it in terms of the classical variable $\alpha_L \equiv \frac{1}{\sqrt{2\lambda}}(u_L^X + iu_L^P)$ [25]

$$\mathcal{H} = \sum_L \omega_L \alpha_L^* \alpha_L + \frac{1}{2}g_L \alpha_L^{*2} + \frac{1}{2}g_L^* \alpha_L^2 - \frac{\gamma}{4\pi} \sum_{L \neq L'} \frac{\alpha_L^* \alpha_{L'} + 3e^{i2\varphi_{LL'}} \alpha_L^* \alpha_{L'}}{|\mathbf{Z}_L^0 - \mathbf{Z}_{L'}^0|^3} + h.c. \quad (3)$$

Here ω_L are the onsite quasienergies, $\omega_L - \omega_0 \sim \mathcal{O}(\gamma)$, and $\varphi_{LL'}$ is the angular coordinate of $\mathbf{Z}_L^0 - \mathbf{Z}_{L'}^0$, cf. Fig. 1(d). The Hamiltonian Eq. (3) describes phonons propagating in our honeycomb phase-space crystal. It is reminiscent of the tight-binding model for electrons in graphene, but with two qualitatively new features: (i) Our phase-space phonons can hop between any two arbitrarily distant sites reflecting the long-range nature of the atom-atom interaction, cf. Fig. 1(d); (ii) The excitation-number is not conserved, because a phonon pair can be created or annihilated on any pair of sites.

Time-reversal and chirality.— The time-reversal transformation changes the chirality of 2D real-space trajectory-

ries, e.g., from clockwise to anti-clockwise. For this reason, robust chiral edge states – without a time-reversed partner with opposite chirality – can be implemented in 2D real space only after breaking the TRS. However, this constraint does not apply to phase-space crystals, because the chirality of motion in phase space remains unchanged under a time-reversal transformation. Indeed, because of the complex phases $\varphi_{LL'}$, Hamiltonian (3) does not support any local anti-unitary symmetry. This is, in fact, the standard formal precondition for non-trivial Chern numbers and chiral edge states [38, 39]. For phase-space crystals, it can be fulfilled even though the time-reversal remains a symmetry, because this symmetry rearranges phase-space crystal in a non-local fashion, i.e., $(X_i, P_i) \rightarrow (X_i, -P_i)$ for all the atoms. It is remarkable that the complex phases $\varphi_{LL'}$ inducing the topological phase have a geometrical interpretation (as the angular coordinate of the vector connecting two attractors). This is a general property of vibrations in phase space valid for any arbitrary phase-space single-particle Hamiltonian $H_s(\mathbf{Z})$ and atom-atom interaction $U(\mathbf{Z}_i - \mathbf{Z}_j)$ [25]. This is in stark contrast to the non-reciprocal phases of tight-binding Hamiltonians in 2D real space which can be tuned without displacing the lattice sites.

Connection to the QAHE.– In the regime where the pairing interaction is off-resonant, for $|\gamma| \ll |\omega_0|$, its main effect is to induce effective hopping transitions with non-reciprocal phases [40], cf. Fig. 1(e). This allows to derive an effective excitation-conserving tight-binding model that differs from the well-known Haldane model for the QAHE [3] only in that it includes long-range hopping transitions [25]. As for the Haldane model, the non-reciprocal hopping phases can be viewed as being induced by an effective staggered magnetic field, cf. Fig. 1(e), and open a small topological gap of width $\sim \gamma^2/\omega_0$ and with band-gap Chern number $C = -1$, cf. Fig. 2(a).

Strong interaction regime.– In the strong interaction regime, $|\gamma| \gg |\omega_0|$, the phonon number is not even approximately conserved and it is, thus, not possible to employ a single-particle description. The physics is also different compared to superconducting systems [41] (with fermionic pairing-interactions): for bosons, there is no limit to the occupation number of single-particle states, which can lead to the amplification of fluctuations and even to instabilities [8, 40, 42].

In the stable regime, the Hamiltonian (3) can be diagonalized via a Bogoliubov transformation [25]. For the bulk, $\mathcal{H} = \sum_{\mathbf{k}, n=1,2} \omega_{\mathbf{k},n} |\beta_{\mathbf{k},n}|^2$ where $\mathbf{k} = (k_X, k_P)$ is the quasi-momentum, $\omega_{\mathbf{k},n}$ is the band structure, and $\beta_{\mathbf{k},n}$ are the normal modes, $\beta_{\mathbf{k},n}^* = \sum_{s=A,B} u_{n,s}(\mathbf{k}) \alpha_{\mathbf{k},s}^* + v_{n,s}(\mathbf{k}) \alpha_{-\mathbf{k},s}$ with $\alpha_{\mathbf{k},s} \equiv \frac{1}{\sqrt{N}} \sum_l \alpha_{l,s} e^{-i\mathbf{k} \cdot \mathbf{Z}_{l,0}^0}$ (N is the number of primitive cells). In this classical setting, the quantization of the Chern number $C = \frac{1}{2\pi} \int_{BZ} (\nabla_{\mathbf{k}} \times \mathcal{A}_n(\mathbf{k})) \cdot \hat{\mathbf{z}}$ with $\mathcal{A}_n(\mathbf{k}) = i \sum_s [u_{1,s}^*(\mathbf{k}) \nabla_{\mathbf{k}} u_{1,s}(\mathbf{k}) - v_{n,s}^*(\mathbf{k}) \nabla_{\mathbf{k}} v_{n,s}(\mathbf{k})]$ [8, 25, 40] follows from the conserva-

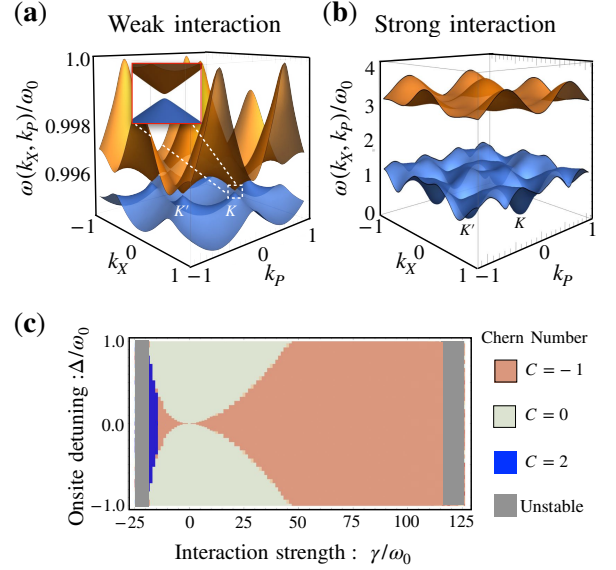


FIG. 2. Bulk band structures for weak interaction strength $\gamma/\omega_0 = -0.2$ (a) and strong interaction $\gamma/\omega_0 = 102$ (b). Topological phase diagram (c) with Chern number C (the Chern number of the lowest band [25]) as a function of interaction strength γ and on-site detuning Δ , which lifts the degeneracy at the K (K') symmetry points.

tion of the Poisson brackets $\{\beta_{\mathbf{k}',n'}^*, \beta_{\mathbf{k},n}\} = i\delta_{n,n'}\delta_{\mathbf{k}',\mathbf{k}}$ (or, equivalently, $\sum_s |u_{n,s}|^2 - |v_{n,s}|^2 = 1$).

The band structure for a comparatively strong interaction is shown in Fig. 2(b). In this case, the Chern number $C = -1$ remains the same as in the weak-interaction limit. We note that close to the K and K' -points (as labelled in the figure) the lowest band approaches zero quasienergy. In the presence of bosonic pairing interactions, the quasienergy can be viewed as the energy cost of producing a pair of Bogoliubov excitations. When this hits zero for a critical threshold $\gamma_c^+ \approx 115\omega_0$ or $\gamma_c^- \approx -20\omega_0$, the phase-space crystal becomes unstable, leading to a disordered gas phase.

Topological phase diagram.– We have systematically investigated our phase-space crystal by varying the interaction strength but also allowing for different onsite quasienergies, $\omega_L \equiv \omega_0 \pm 2\Delta$, for the two honeycomb sublattices. The onsite detuning Δ (engineered using additional stroboscopic lasers [25]) breaks the inversion symmetry, allowing a trivial band gap [3]. The ensuing topological phase diagram is shown in Fig. 2(c). For $\Delta = 0$, the phase-space crystal has Chern number $C = -1$ for a broad range of positive and negative γ/ω_0 , but can also switch to $C = 2$ for negative γ/ω_0 , before becoming unstable. The $C = 2$ topological phase is not present in the Haldane model [3]. In the region of weak interactions, the band edge is cone-shaped and the band gap scales as γ^2/ω_0 for $\Delta = 0$. In this regime, the gap determines how far the topological region extends into the $\Delta \neq 0$ region.

Topological transport.– Before investigating a realistic

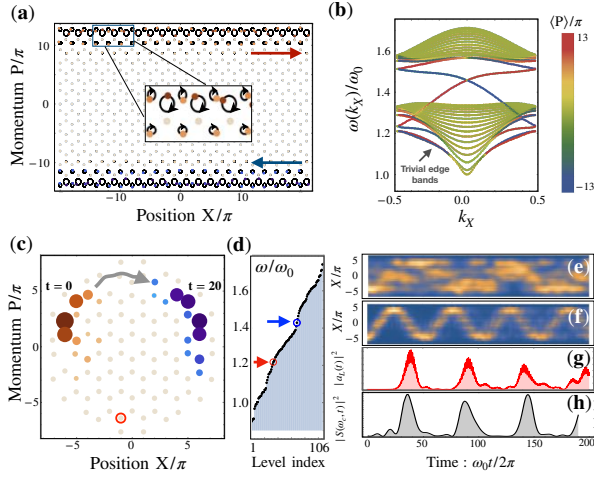


FIG. 3. **Topological edge states.** (a) Strip-shaped phase-space crystal with two topological edge states propagating on the boundaries. Inset shows atoms' orbits (circles) and vibration energy (colour). (b) Band structure of the strip with colour indicating the average P of each eigenstate. (c) Disk-shaped phase-space crystal with random defects on the edge. We show one edge channel wave packet at different temporal instants. (d) Energy spectrum with arrows indicating the energy level centres for constructing the wave packet in (c) by the Gaussian superposition of eigenstates. (e)-(f) Spacetime plot of wave packet, projected on the spatial X dimension. The central frequencies ω_c of wave packets in (e) and (f) are indicated by the red and blue arrows in (d) respectively. (g) Vibration $|a_L(t)|^2$ of the atom marked by red circle in (c). (h) Finite-time-window power spectrum $S(\omega_c, t)$ of a collective signal from all the atoms. [Parameters: interaction $\gamma = 25\omega_0$ for all figures; disk radius $R = 8\pi$ and $\delta\omega = 1.35\sigma\pi R^{-1}$ for (c)-(g); time window $\Delta t = 10 \times 2\pi\omega_0^{-1}$ for (g)]

disk-shaped phase-space crystal, we consider a conceptually simpler strip geometry, cf Fig. 3(a). For simplicity we neglect the interaction-induced (slight) deformation of the equilibrium configuration. We plot the resulting strip band structure in Fig. 3(b), for parameters in the topological phase $C = -1$. As usual for Chern insulators, the edge states on opposite physical boundaries have opposite propagation direction and, thus, the same chirality, Fig. 3(a-b). However, in contrast to a standard 2D Chern insulator, here, they are mapped onto each other via the non-local time-reversal transformation in phase space.

We now turn to a realistic disk-shaped crystal with a randomly-shaped boundary [Fig. 3(c)]. Here, we fully take into account the atom-atom interaction that deforms the equilibrium configuration. As discussed above, one can reduce the deformation using a finite laser detuning $\delta\omega$ in Eq. (1) [25]. In Fig. 3(c), we illustrate the chiral transport by tracking the time evolution of a wave packet with average quasienergy ω_c in the middle of the band gap, cf. blue arrow in Fig. 3(d). It can be readily observed that the transport is robust against the boundary defects [43]. In Figs. 3(e)-(f), we com-

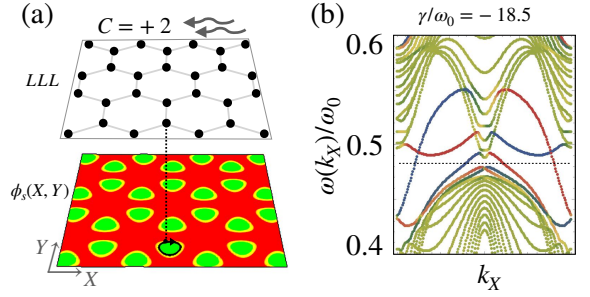


FIG. 4. **Real-space implementation for ions or semiconductor electrons - vibrations of cyclotron guiding centres.** (a) Cyclotron orbital centres (upper panel) in LLL subjected to an external honeycomb lattice potential $\phi_s(X, Y)$ (lower panel). (b) Band structure of strip-shhaped geometry for interaction parameter $\gamma/\omega_0 = -18.5$, where the Chern number of corresponding bulk band is $C = +2$.

pare the non-chiral and chiral transports by projecting the evolution of the wave packet onto the coordinate X in the rotating frame. The time evolution of a single atom's vibrational energy likewise reveals the periodicity of the packet traversing the disk's circumference, cf. Fig. 3(g). However, in any real experiment, it might be easier to obtain a collective signal from all the atoms, for example by light scattering: $I(t) = \sum_j \cos[k_s X_j(t)]$ interpreted by using a stroboscopic optical lattice for detection. One can extract the finite-time-window power spectrum $S(\omega, t) \propto \left| \left\langle (I(t) - \langle I \rangle) e^{i\omega t} \right\rangle_{\Delta t} \right|^2$, where $\langle \dots \rangle_{\Delta t}$ represents the time average over a finite time window. In Fig. 3(h), we plot the power spectrum $S(\omega_c, t)$ (at $k_s = 8.55$) as a function of time. The periodic temporal peaks of S nicely indicate the chiral motion of the wave packet (see experimental parameters in SM [25]).

Implications for real space motion- The phase-space dynamics investigated here could also be realized in 2D real space using ions in a magnetic field. In an out-of-plane magnetic field $\mathbf{B} = B\hat{n}$, the motion of the ions can be decomposed into the cyclotron motion and the drift of the cyclotron guiding center. The two guiding center coordinates $\mathbf{Z} = (X, Y)$ constitute an effective phase space ($[X, Y] = -i\hbar/qB$ in quantum mechanics) [44]. If all the relevant energy scales are much smaller than the cyclotron energy $\hbar\omega_c = \hbar|q|B/m$, the motion is frozen into the lowest Landau level (LLL). The classical dynamics of the guiding center is governed by $\dot{\mathbf{Z}}_i = (qB)^{-1} \mathbf{F}_i \times \hat{n}$, similar to the phase-space dynamics, cf. discussion below Eq. (2). Considering that the phase-space interaction Eq. (2) has the Coulomb form, our model is implemented in the 2D external electrostatic potential $\phi_s(\mathbf{Z}) \propto H_s(\mathbf{Z})$, cf. Eq. (1). We note that for filling factors $\nu \equiv 2\pi n\hbar/eB$ (where n is the density) below a critical threshold ν_w , the ground state of the ions is expected to be a crystal even without any external confining potential [45, 46], a so-called Wigner Crystal [47, 48].

However, in this case the guiding centers are known to be arranged on a simple Bravais triangular lattice, leading to a single trivial phonon band [48–50]. Our work shows that when the guiding centers are rearranged on a honeycomb lattice by an external electrostatic potential, the crystal vibrations become topological. In this context, it is instructive to revisit our results in Fig. 2. The presence of topological phases with different sign of the Chern number C indicates that the chirality of the vibrations can be reversed. Counterintuitively, for $C = 2$ corresponding to strong repulsive interactions γ , the chirality of the phonon edge states is opposite compared to the chirality of the cyclotron orbits.

Outlook—Robust topology produced by the combination of symplectic phase-space geometry and interactions represents a versatile concept that can be implemented in many physical platforms. For atoms with spin, one would obtain nonlocal spin-dependent interactions in phase space [15, 51], coupling spin waves to topological phase-space phonons. Long-range real-space interactions permit the exploration of higher-dimensional generalizations of the physics discussed here in 1D. More complex driving can be used to synthesize arbitrary phase-space potentials [52], and single-shot measurements of multi-atom configurations will allow the observation of additional effects like nonlinear evolution.

Acknowledgements

We acknowledge helpful discussions with Tirth Shah and Herrmann Schulz-Baldes.

-
- [1] K. v. Klitzing, G. Dorda, and M. Pepper, “New method for high-accuracy determination of the fine-structure constant based on quantized hall resistance,” *Phys. Rev. Lett.* **45**, 494–497 (1980).
 - [2] M. Z. Hasan and C. L. Kane, “Colloquium: Topological insulators,” *Rev. Mod. Phys.* **82**, 3045–3067 (2010).
 - [3] F. D. M. Haldane, “Model for a quantum hall effect without landau levels: Condensed-matter realization of the “parity anomaly”,” *Phys. Rev. Lett.* **61**, 2015–2018 (1988).
 - [4] F. D. M. Haldane and S. Raghu, “Possible realization of directional optical waveguides in photonic crystals with broken time-reversal symmetry,” *Phys. Rev. Lett.* **100**, 013904 (2008).
 - [5] Ling Lu, John D. Joannopoulos, and Marin Soljačić, “Topological photonics,” *Nature Photonics* **8**, 821–829 (2014).
 - [6] Tomoki Ozawa, Hannah M. Price, Alberto Amo, Nathan Goldman, Mohammad Hafezi, Ling Lu, Mikael C. Rechtsman, David Schuster, Jonathan Simon, Oded Zilberberg, and Iacopo Carusotto, “Topological photonics,” *Rev. Mod. Phys.* **91**, 015006 (2019).
 - [7] Hosho Katsura, Naoto Nagaosa, and Patrick A. Lee, “Theory of the thermal hall effect in quantum magnets,” *Phys. Rev. Lett.* **104**, 066403 (2010).
 - [8] Ryuichi Shindou, Ryo Matsumoto, Shuichi Murakami, and Jun-ichiro Ohe, “Topological chiral magnonic edge mode in a magnonic crystal,” *Phys. Rev. B* **87**, 174427 (2013).
 - [9] V. Peano, C. Brendel, M. Schmidt, and F. Marquardt, “Topological phases of sound and light,” *Phys. Rev. X* **5**, 031011 (2015).
 - [10] Hussein Nassar, Behrooz Yousefzadeh, Romain Fleury, Massimo Ruzzene, Andrea Alù, Chiara Daraio, Andrew N. Norris, Guoliang Huang, and Michael R. Haberman, “Nonreciprocity in acoustic and elastic materials,” *Nature Reviews Materials* **5**, 667–685 (2020).
 - [11] Jean Dalibard, Fabrice Gerbier, Gediminas Juzeliūnas, and Patrik Öhberg, “Colloquium: Artificial gauge potentials for neutral atoms,” *Rev. Mod. Phys.* **83**, 1523–1543 (2011).
 - [12] N Goldman, G Juzeliūnas, P Öhberg, and I B Spielman, “Light-induced gauge fields for ultracold atoms,” *Reports on Progress in Physics* **77**, 126401 (2014).
 - [13] Lingzhen Guo, Michael Marthaler, and Gerd Schön, “Phase space crystals: A new way to create a quasienergy band structure,” *Phys. Rev. Lett.* **111**, 205303 (2013).
 - [14] Yaxing Zhang, J. Gosner, S. M. Girvin, J. Ankerhold, and M. I. Dykman, “Time-translation-symmetry breaking in a driven oscillator: From the quantum coherent to the incoherent regime,” *Phys. Rev. A* **96**, 052124 (2017).
 - [15] Pengfei Liang, Michael Marthaler, and Lingzhen Guo, “Floquet many-body engineering: topology and many-body physics in phase space lattices,” *New Journal of Physics* **20**, 023043 (2018).
 - [16] Niels Lörch, Yaxing Zhang, Christoph Bruder, and M. I. Dykman, “Quantum state preparation for coupled period tripling oscillators,” *Phys. Rev. Research* **1**, 023023 (2019).
 - [17] P. Leboeuf, J. Kurchan, M. Feingold, and D. P. Arovas, “Phase-space localization: Topological aspects of quantum chaos,” *Phys. Rev. Lett.* **65**, 3076–3079 (1990).
 - [18] P. Leboeuf, J. Kurchan, M. Feingold, and D. P. Arovas, “Topological aspects of quantum chaos,” *Chaos: An Interdisciplinary Journal of Nonlinear Science* **2**, 125–130 (1992).
 - [19] Netanel H. Lindner, Gil Refael, and Victor Galitski, “Floquet topological insulator in semiconductor quantum wells,” *Nature Physics* **7**, 490–495 (2011).
 - [20] Mark S. Rudner, Netanel H. Lindner, Erez Berg, and Michael Levin, “Anomalous edge states and the bulk-edge correspondence for periodically driven two-dimensional systems,” *Phys. Rev. X* **3**, 031005 (2013).
 - [21] A. Celi, P. Massignan, J. Ruseckas, N. Goldman, I. B. Spielman, G. Juzeliūnas, and M. Lewenstein, “Synthetic gauge fields in synthetic dimensions,” *Phys. Rev. Lett.* **112**, 043001 (2014).
 - [22] Tomoki Ozawa and Hannah M. Price, “Topological quantum matter in synthetic dimensions,” *Nature Reviews Physics* **1**, 349–357 (2019).
 - [23] Luqi Yuan, Qian Lin, Meng Xiao, and Shanhui Fan, “Synthetic dimension in photonics,” *Optica* **5**, 1396–1405 (2018).
 - [24] Dominik Suszalski and Jakub Zakrzewski, “Different lattice geometries with a synthetic dimension,” *Phys. Rev. A* **94**, 033602 (2016).
 - [25] “See the details in the supplemental material,” .
 - [26] G. M. Zaslavsky, Zakharov M. Yu., R. Z. Sagdeev, D. A.

- Usikov, and A. A. Chernikov, “Stochastic web and diffusion of particles in a magnetic field,” *Zh. Eksp. Teor. Fiz.* **91**, 500 (1986).
- [27] F. L. Moore, J. C. Robinson, C. F. Bharucha, Bala Sundaram, and M. G. Raizen, “Atom optics realization of the quantum δ -kicked rotor,” *Phys. Rev. Lett.* **75**, 4598–4601 (1995).
- [28] Julien Chabé, Gabriel Lemarié, Benoît Grémaud, Dominique Delande, Pascal Szriftgiser, and Jean Claude Garreau, “Experimental observation of the anderson metal-insulator transition with atomic matter waves,” *Phys. Rev. Lett.* **101**, 255702 (2008).
- [29] Isam Manai, Jean-François Clément, Radu Chicireanu, Clément Hainaut, Jean Claude Garreau, Pascal Szriftgiser, and Dominique Delande, “Experimental observation of two-dimensional anderson localization with the atomic kicked rotor,” *Phys. Rev. Lett.* **115**, 240603 (2015).
- [30] Gabriela B. Lemos, Rafael M. Gomes, Stephen P. Walborn, Paulo H. Souto Ribeiro, and Fabricio Toscano, “Experimental observation of quantum chaos in a beam of light,” *Nature Communications* **3**, 1211 (2012).
- [31] G. M. Zaslavsky, *A Hamiltonian Chaos and Fractional Dynamics* (Oxford University Press, Oxford, 2008).
- [32] Immanuel Bloch, Jean Dalibard, and Wilhelm Zwerger, “Many-body physics with ultracold gases,” *Rev. Mod. Phys.* **80**, 885–964 (2008).
- [33] K. Sacha, “Anderson localization and mott insulator phase in the time domain,” *Sci. Rep.* **5**, 10787 (2015).
- [34] Krzysztof Sacha, “Modeling spontaneous breaking of time-translation symmetry,” *Phys. Rev. A* **91**, 033617 (2015).
- [35] Lingzhen Guo, Modan Liu, and Michael Marthaler, “Effective long-distance interaction from short-distance interaction in a periodically driven one-dimensional classical system,” *Phys. Rev. A* **93**, 053616 (2016).
- [36] Krzysztof Giergiel, Artur Miroszewski, and Krzysztof Sacha, “Time crystal platform: From quasicrystal structures in time to systems with exotic interactions,” *Phys. Rev. Lett.* **120**, 140401 (2018).
- [37] Edward Ott, *Chaos in Dynamical Systems (2nd Edition)* (Cambridge University Press, The Edinburgh Building, Cambridge CB2 8RU, UK, 2002).
- [38] Christian Brouder, Gianluca Panati, Matteo Calandra, Christophe Mourougane, and Nicola Marzari, “Exponential localization of wannier functions in insulators,” *Phys. Rev. Lett.* **98**, 046402 (2007).
- [39] Ching-Kai Chiu, Jeffrey C. Y. Teo, Andreas P. Schnyder, and Shinsei Ryu, “Classification of topological quantum matter with symmetries,” *Rev. Mod. Phys.* **88**, 035005 (2016).
- [40] Vittorio Peano, Martin Houde, Christian Brendel, Florian Marquardt, and Aashish A. Clerk, “Topological phase transitions and chiral inelastic transport induced by the squeezing of light,” *Nature Communications* **7**, 10779 (2016).
- [41] Panagiotis Kotetes, “Classification of engineered topological superconductors,” *New Journal of Physics* **15**, 105027 (2013).
- [42] Charles-Edouard Bardyn, Torsten Karzig, Gil Refael, and Timothy C. H. Liew, “Chiral bogoliubov excitations in nonlinear bosonic systems,” *Phys. Rev. B* **93**, 020502 (R) (2016).
- [43] “See the animation in the supplemental video,” .
- [44] J. Zak, “Balian-low theorem for landau levels,” *Phys. Rev. Lett.* **79**, 533–536 (1997).
- [45] R. B. Laughlin, “Anomalous quantum hall effect: An incompressible quantum fluid with fractionally charged excitations,” *Phys. Rev. Lett.* **50**, 1395–1398 (1983).
- [46] V. J. Goldman, M. Shayegan, and D. C. Tsui, “Evidence for the fractional quantum hall state at $\nu = \frac{1}{7}$,” *Phys. Rev. Lett.* **61**, 881–884 (1988).
- [47] E. Wigner, “On the interaction of electrons in metals,” *Phys. Rev.* **46**, 1002–1011 (1934).
- [48] Joonho Jang, Benjamin M. Hunt, Loren N. Pfeiffer, Kenneth W. West, and Raymond C. Ashoori, “Sharp tunnelling resonance from the vibrations of an electronic wigner crystal,” *Nature Physics* **13**, 340–344 (2017).
- [49] Lynn Bonsall and A. A. Maradudin, “Some static and dynamical properties of a two-dimensional wigner crystal,” *Phys. Rev. B* **15**, 1959–1973 (1977).
- [50] René Côté and A. H. MacDonald, “Phonons as collective modes: The case of a two-dimensional wigner crystal in a strong magnetic field,” *Phys. Rev. Lett.* **65**, 2662–2665 (1990).
- [51] Lingzhen Guo and Pengfei Liang, “Condensed matter physics in time crystals,” *New Journal of Physics* **22**, 075003 (2020).
- [52] Lingzhen Guo, Vittorio Peano, and Marquardt Florian, in preparation.
- [53] T. P. Billam and S. A. Gardiner, *Phys. Rev. A* **80**, 023414 (2009).
- [54] B. Paredes, A. Widera, V. Murg, O. Mandel, S. Fölling, I. Cirac, G. V. Shlyapnikov, T. W. Hänsch, and I. Bloch, *Nature* **429**, 277 (2004).
- [55] H. Moritz, T. Stöferle, M. Köhl, and T. Esslinger, *Phys. Rev. Lett.* **91**, 250402 (2003).
- [56] Z. Hadzibabic, S. Stock, B. Battelier, V. Bretin, and J. Dalibard, *Phys. Rev. Lett.* **93**, 180403 (2004).
- [57] K. B. Davis, M. O. Mewes, M. R. Andrews, N. J. van Druten, D. S. Durfee, D. M. Kurn, and W. Ketterle, *Phys. Rev. Lett.* **75**, 3969 (1995).
- [58] E. A. Cornell and C. E. Wieman, *Rev. Mod. Phys.* **74**, 875 (2002).
- [59] D. G. Greif, Master thesis, (2007), URL http://ultracold.physics.sunysb.edu/subpages/pubfiles/Greif_MA2007.pdf.

**SUPPLEMENTAL MATERIAL FOR
PHASE SPACE CRYSTAL VIBRATIONS:
CHIRAL EDGE STATES WITH PRESERVED TIME-REVERSAL SYMMETRY**

I. Phase-space lattice Hamiltonian

General form

We discuss how to synthesize arbitrary lattice structures in phase space via multiple stroboscopic lattices. We start from the following generalised model of kicked harmonic oscillator

$$H_s = \frac{1}{2}(x^2 + p^2) + \sum_{n \in \mathbb{Z}} \sum_q K_q \cos(k_q x - \phi_q) \delta\left(\frac{t}{\tau} - \theta_q - n\right). \quad (4)$$

Here q represents the kicking sequence of stroboscopic lattices whose intensity K_q , wave vector k_q and phase ϕ_q can be tuned at different time instances $t = \tau(n + \theta_q)$ with $n \in \mathbb{Z}$. To simplify the discussion, we first consider a single kick,

$$H_s = \frac{1}{2}(x^2 + p^2) + K_q \cos(k_q x - \phi_q) \delta\left(\frac{t}{\tau} - \theta_q - n\right). \quad (5)$$

We transform the above Hamiltonian into rotating frame with kicking frequency $2\pi/\tau$ using the generating function of the second kind

$$G_2(x, P, t) = \frac{xP}{\cos(2\pi t/\tau)} - \frac{1}{2}x^2 \tan\left(\frac{2\pi}{\tau}t\right) - \frac{1}{2}P^2 \tan\left(\frac{2\pi}{\tau}t\right). \quad (6)$$

The corresponding canonical transformation is given by

$$p = \frac{\partial G_2}{\partial x}, \quad X = \frac{\partial G_2}{\partial P}, \quad H_s(X, P, t) = H_s(x, p, t) + \frac{\partial G_2}{\partial t},$$

which results in the transformation of phase-space coordinates

$$x = P \sin\left(\frac{2\pi t}{\tau}\right) + X \cos\left(\frac{2\pi t}{\tau}\right), \quad p = P \cos\left(\frac{2\pi t}{\tau}\right) - X \sin\left(\frac{2\pi t}{\tau}\right) \quad (7)$$

and the transformed Hamiltonian

$$H_s(X, P, t) = \frac{1}{2}\delta\omega(X^2 + P^2) + K_q \cos\left[k_q\left(P \sin\frac{2\pi t}{\tau} + X \cos\frac{2\pi t}{\tau}\right) - \phi_q\right] \delta\left(\frac{t}{\tau} - \theta_q - n\right). \quad (8)$$

Here, we have defined the global detuning parameter $\delta\omega \equiv 1 - 2\pi/\tau$ between kicking and harmonic oscillation. For weak resonant driving ($|K_q| \ll 1$, $\delta\omega = 0$), the single-particle dynamics can be separated by the fast harmonic oscillation and the low motion of its quadratures (X, P) . The effective slow dynamics of quadratures (X, P) is given by the lowest-order Magnus expansion, i.e., the time average of $H_s(X, P, t)$ in one kicking time period,

$$H_s(X, P) = \frac{1}{\tau} \int_0^\tau H_s(X, P, t) dt = K_q \cos\left[k_q\left(P \sin 2\pi\theta_q + X \cos 2\pi\theta_q\right) - \phi_q\right]. \quad (9)$$

The above derivation is for classical dynamics. For quantum dynamics, the result has the same form with replacing X and P by their operators [15, 53]. Extending the result for single kick to all kicks in Eq. (4), we obtain the general form of phase-space lattice Hamiltonian

$$H_s(X, P) = \sum_q K_q \cos\left[k_q\left(P \sin 2\pi\theta_q + X \cos 2\pi\theta_q\right) - \phi_q\right]. \quad (10)$$

In principle, any arbitrary lattice Hamiltonian in phase space can be synthesized by multiple stroboscopic lattices.

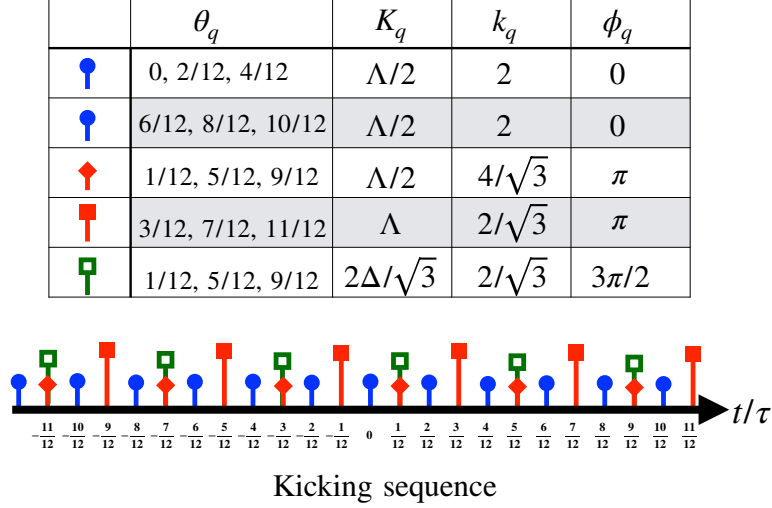


FIG. 5. Kicking parameters for generating honeycomb phase space lattice Hamiltonian. Below the parameter table, we show the corresponding kicking sequence, which preserves a time-reversal symmetry if the reference time point is shifted by $\tau/12$.

Honeycomb phase-space lattice

For the honeycomb lattice considered in our work, we can get the desired driving parameters by decomposing the honeycomb lattice into a series of cosine functions, i.e.,

$$\begin{aligned}
 H_s(X, P) &= 16\Lambda \sin^2\left(\frac{1}{2}X + \frac{1}{2\sqrt{3}}P\right) \sin^2\left(-\frac{1}{2}X + \frac{1}{2\sqrt{3}}P\right) \sin^2\left(\frac{1}{\sqrt{3}}P\right) \\
 &= \Lambda \left(\frac{3}{2} + \cos[2(X \cos 0 + P \sin 0)] \right. \\
 &\quad + \cos[2(X \cos \frac{\pi}{3} + P \sin \frac{\pi}{3})] + \cos[2(X \cos \frac{2\pi}{3} + P \sin \frac{2\pi}{3})] \\
 &\quad + \frac{1}{2} \cos[\frac{4}{\sqrt{3}}(X \cos \frac{\pi}{6} + P \sin \frac{\pi}{6}) - \pi] + \frac{1}{2} \cos[\frac{4}{\sqrt{3}}(X \cos \frac{5\pi}{6} + P \sin \frac{5\pi}{6}) - \pi] \\
 &\quad + \frac{1}{2} \cos[\frac{4}{\sqrt{3}}(X \cos \frac{3\pi}{2} + P \sin \frac{3\pi}{2}) - \pi] \\
 &\quad + \cos\left[\frac{2}{\sqrt{3}}(X \cos \frac{\pi}{2} + P \sin \frac{\pi}{2}) - \pi\right] + \cos\left[\frac{2}{\sqrt{3}}(X \cos \frac{7\pi}{6} + P \sin \frac{7\pi}{6}) - \pi\right] \\
 &\quad \left. + \cos\left[\frac{2}{\sqrt{3}}(X \cos \frac{11\pi}{6} + P \sin \frac{11\pi}{6}) - \pi\right] \right). \tag{11}
 \end{aligned}$$

Comparing the above expansion to Eq. (10), we can generate the honeycomb phase space Hamiltonian (up to a constant $3\Lambda/2$) by choosing the kicking parameters and kicking sequence given in Fig. 5. The extrema of $H_s(X, P)$ represent stable points of the classical dynamics. The small vibrations about these stable points have frequency $\omega_0 = -9\Lambda$ from the linear expansion of Eq. (11). We rewrite the honeycomb lattice Hamiltonian in form of

$$H_s(\mathbf{Z}) = -\frac{16}{9}\omega_0 \prod_{n=1}^3 \sin^2\left(\frac{1}{2}\mathbf{v}_n \cdot \mathbf{Z}\right), \tag{12}$$

where we have defined the vector $\mathbf{Z} \equiv (X, P)$ and three ancillary vectors $\mathbf{v}_1 = (1, \frac{1}{\sqrt{3}})$, $\mathbf{v}_2 = (-1, \frac{1}{\sqrt{3}})$, $\mathbf{v}_3 = (0, -\frac{2}{\sqrt{3}})$. The two sublattices of the phase-space honeycomb lattice Hamiltonian (12) have the same vibration frequency at their lattice sites.

One can also tune the on-site frequencies of two sublattices with the following phase space lattice Hamiltonian

$$H_s^\Delta = -\frac{2\Delta}{\sqrt{3}} \sum_{n=1}^3 \sin(\mathbf{v}_n \cdot \mathbf{Z}) = \frac{2\Delta}{\sqrt{3}} \sum_{n=1}^3 \cos(\mathbf{v}_n \cdot \mathbf{Z} - \frac{3\pi}{2}), \quad (13)$$

which can be implemented by additional stroboscopic lattices with kicking parameters $K_q = 2\Delta/\sqrt{3}$, $k_q = 2/\sqrt{3}$ and $\phi_q = 3\pi/2$ for $\theta_q = 1/12, 5/12, 9/12$ as shown in Fig. 5. The on-site frequencies of two sublattices are then $\omega_0 \pm 2\Delta$ with the parameter Δ which we call the *on-site detuning*. Finally, the total single-particle Hamiltonian of honeycomb lattice including the on-site detuning terms is given by

$$H_s(\mathbf{Z}) = \frac{1}{2}\delta\omega|\mathbf{Z}|^2 - \frac{16}{9}\omega_0 \prod_{n=1}^3 \sin^2\left(\frac{1}{2}\mathbf{v}_n \cdot \mathbf{Z}\right) - \frac{2\Delta}{\sqrt{3}} \sum_{n=1}^3 \sin(\mathbf{v}_n \cdot \mathbf{Z}). \quad (14)$$

Here we have also included the global detuning given by Eq. (8).

Time-reversal symmetry

Adding a driving field into a static Hamiltonian does not necessarily breaks time-reversal symmetry. If the time-dependent Hamiltonian is an even function of time (with respect to a proper reference time point) $H(t) = H(-t)$, the system still preserves time-reversal symmetry. More strictly speaking, if $\mathbf{Z}(t) \equiv (x(t), p(t))$ satisfies the following Hamiltonian equation of motion

$$\frac{dx(t)}{dt} = \frac{\partial H(x(t), p(t), t)}{\partial p(t)}, \quad \frac{dp(t)}{dt} = -\frac{\partial H(x(t), p(t), t)}{\partial x(t)},$$

the time-reversal partner $\mathbf{Z}'(t) \equiv (x(-t), -p(-t))$ is also the solution of the same Hamiltonian equation given that $H(x, p, t) = H(x, -p, -t)$. In Fig. 5, we show the kicking sequence below the parameter table to generate a honeycomb lattice Hamiltonian. It is clear that the kicking sequence preserves time-reversal symmetry if the reference point of time is shifted by $\tau/12$. Therefore, our model indeed preserves time-reversal symmetry.

From the canonical transformation (7), the phase space Hamiltonian $H_s(X, P)$ describes the stroboscopic dynamics of $H_s(x, p)$ in the lab frame with stroboscopic time period $\Delta t = \tau$. Shifting a time reference point by $\tau/12$ in the kicking sequence merely means the stroboscopic time steps are also shifted by $\tau/12$ accordingly, i.e., $t = \tau/12 + n\tau$ ($n \in \mathbb{Z}$). Under this choice, the time-reversal transformation in the lab frame $(x(t), p(t)) \rightarrow (x(-t), -p(-t))$ has the same form in the stroboscopic dynamics $(X(t), P(t)) \rightarrow (X(-t), -P(-t))$, which is a nonlocal transformation in the (X, P) phase space since it includes a mirror operation with respect to $X = 0$. This is the choice we adopt throughout our paper. If other reference time point is chosen for stroboscopic dynamics, the time-reversal transformation of (x, p) corresponds to a more complex transformation of quadratures (X, P) , in which the axial of mirror operation in (X, P) phase space is rotated by an angle.

II. Many-body Hamiltonian

We consider many interacting particles trapped in the same 1D harmonic potential. The interaction $V(x_i - x_j)$ induces an effective interaction of two particles on their quadratures [15, 33–35]. The general method to extract this effective interaction in phase space has been developed in Refs. [15, 35]. The interaction of cold atoms due to the s -wave scattering is a point-like contact interaction $V(x_i - x_j) = \gamma\delta(x_i - x_j)$. The effective phase-space interaction potential is a Coulomb-like interaction $U(R_{ij}) = \gamma\pi^{-1}R_{ij}^{-1}$, where

$$R_{ij} \equiv \sqrt{(X_i - X_j)^2 + (P_i - P_j)^2} = |\mathbf{Z}_i - \mathbf{Z}_j|$$

is the phase-space distance between two atoms i and j . The effective phase space interaction is valid for well-separated atoms which is the case of phase space crystals considered in this work [15, 35]. Finally, we have the many-body Hamiltonian for this work

$$H = \sum_L H_s(X_L, P_L) + \frac{1}{2} \sum_{L \neq L'} U(R_{LL'}) \equiv T + \Phi. \quad (15)$$

Here, we have relabelled the atoms by the subscript $L = (l, s)$ representing the l -th atom in the $s \in \{A, B\}$ sublattice. $T \equiv \sum_L H_s(X_L, P_L)$ is the total single-particle contribution and $\Phi \equiv \frac{1}{2} \sum_{L \neq L'} U(R_{LL'})$ the total interaction part.

Equilibrium configuration

In the presence of the lattice potential and their effective interaction, the atoms have equilibrium configuration in phase space. The equilibrium points of atoms $\mathbf{Z}_L^0 = (X_L^0, P_L^0)$ are determined by the condition

$$\left. \frac{\partial H}{\partial X_L} \right|_{(X_L^0, P_L^0)} = 0, \quad \left. \frac{\partial H}{\partial P_L} \right|_{(X_L^0, P_L^0)} = 0, \quad (16)$$

where H is the many-body Hamiltonian (15). For the periodic boundaries in both X and P directions, the interactions from symmetric directions cancel each other and the equilibrium points are given by the honeycomb lattice sites. The periodic boundary is helpful for theoretical study. In the real experimental setup, however, the equilibrium positions of atoms will deviate from the lattice sites due to the open boundary of phase space crystal. In fact, the atoms tend to relax towards the stable points and concentrate about the origin of the phase space due to the presence of dissipation. By introducing a relative strong repulsive interaction ($\gamma > 0$), the atoms will spread over the phase space and form a disk-shaped crystal state as shown by Fig. 1(c) in the main text. Note that the interaction of the atoms on the disk will tend to distort the honeycomb equilibrium configuration. There is a mean-field potential induced by the interaction. The effective potential generated by the disk crystal in phase space can be approximated by the Coulomb potential on a uniformly charged disk plane (up to a constant due to the discretisation)

$$\bar{U}(\mathbf{Z}_i) = 2\pi\sigma R \left[1 - \sum_{l=0}^{\infty} (2l+1) \left[\frac{(2l-1)!!}{(2l+2)!!} \right]^2 \left(\frac{|\mathbf{Z}_i|}{R} \right)^{2l+2} \right], \quad (17)$$

where R is the radius of disk, $|\mathbf{Z}_i| < R$ is the phase space distance to the original point of an atom on the disk, and $\sigma = \gamma/\sqrt{3}\pi^3$ is the effective charge density. The leading term ($l=0$) in Eq. (17) produces a harmonic potential $\bar{U}(|\mathbf{Z}_i|) \sim -\sigma\pi R^{-1}|\mathbf{Z}_i|^2/2$. Considering contribution from high-order l -th terms in Eq. (17), we find a better fitting with parabolic function gives

$$\bar{U}(|\mathbf{Z}_i|) \sim -1.35\sigma\pi R^{-1}|\mathbf{Z}_i|^2/2. \quad (18)$$

Therefore, we can introduce an additional global detuning term $1.35\sigma\pi R^{-1}|\mathbf{Z}|^2/2$ in the single-particle Hamiltonian (14), to strongly counterbalance the interaction-induced mean-field potential.

Hamiltonian of phase-space lattice waves

We expand the total many-body Hamiltonian (15) around the equilibrium positions of atoms, i.e., $\mathbf{Z}_L(t) = \mathbf{Z}_L^0 + \mathbf{u}_L(t)$ where $\mathbf{u}_L = (u_L^X, u_L^P)$ is the displacement on the lattice site L . To the second order, the many-body Hamiltonian is given by (up to a constant)

$$H = \frac{1}{2} \sum_{\alpha, \beta} \sum_{L, L'} \eta_{\alpha\beta}^{LL'} u_L^\alpha u_{L'}^\beta, \quad (19)$$

with the matrix $\eta_{\alpha\beta}^{LL'}$ given by

$$\eta_{\alpha\beta}^{LL'} = \left. \frac{\partial^2 H}{\partial u_L^\alpha \partial u_{L'}^\beta} \right|_{\mathbf{0}} = T_{\alpha\beta}^{LL'} + \Phi_{\alpha\beta}^{LL'}. \quad (20)$$

We call $\eta_{\alpha\beta}^{LL'}$ the *phase space force matrix*, which means the resultant force along α direction exerted on the L -th atom due to the unit displacement along β direction of the L' -th atom. The contribution to $\eta_{\alpha\beta}^{LL'}$ from the single-particle Hamiltonian (14) is

$$T_{\alpha\beta}^{LL'} = \left. \frac{\partial^2 H_s}{\partial u_L^\alpha \partial u_{L'}^\beta} \right|_{\mathbf{0}} = \left. \frac{\partial^2 H_s}{\partial u_L^\alpha \partial u_L^\beta} \right|_{\mathbf{0}} \delta_{LL'} = T_{\alpha\beta}^{LL} \delta_{LL'} = (\omega_0 \pm 2\Delta) \delta_{\alpha\beta} \delta_{LL'}. \quad (21)$$

The contribution from interaction part can be obtained by calculating the derivative of interaction potential

$$\frac{\partial \Phi}{\partial Z_L^\alpha} = \sum_{L' \neq L} \frac{U'(R_{LL'})}{R_{LL'}} \left[(X_L - X_{L'}) \delta_{X\alpha} + (P_L - P_{L'}) \delta_{P\alpha} \right]. \quad (22)$$

For two different atoms at different lattice sites ($L \neq L'$), we have the second derivative

$$\begin{aligned}\Phi_{\alpha\beta}^{LL'} &= \frac{\partial^2 \Phi}{\partial Z_L^\alpha \partial Z_{L'}^\beta} \\ &= \frac{U'(R_{LL'})}{R_{LL'}} (-\delta_{X\alpha} \delta_{X\beta} - \delta_{P\alpha} \delta_{P\beta}) + \frac{U''(R_{LL'}) R_{LL'} - U'(R_{LL'})}{R_{LL'}^3} \\ &\quad \times \left[-(X_L - X_{L'}) \delta_{X\beta} - (P_L - P_{L'}) \delta_{P\beta} \right] \left[(X_L - X_{L'}) \delta_{X\alpha} + (P_L - P_{L'}) \delta_{P\alpha} \right].\end{aligned}\quad (23)$$

For the atom at the single lattice site ($L = L'$), we have the second derivative

$$\begin{aligned}\Phi_{\alpha\beta}^{LL} &= \frac{\partial^2 \Phi}{\partial Z_L^\alpha \partial Z_L^\beta} \\ &= \sum_{L' \neq L} \frac{U'(R_{LL'})}{R_{LL'}} (\delta_{X\alpha} \delta_{X\beta} + \delta_{P\alpha} \delta_{P\beta}) + \frac{U''(R_{LL'}) R_{LL'} - U'(R_{LL'})}{R_{LL'}^3} \\ &\quad \times \left[(X_L - X_{L'}) \delta_{X\beta} + (P_L - P_{L'}) \delta_{P\beta} \right] \left[(X_L - X_{L'}) \delta_{X\alpha} + (P_L - P_{L'}) \delta_{P\alpha} \right] \\ &= \sum_{L' \neq L} (-1) \times \frac{\partial^2 \Phi}{\partial Z_{L'}^\beta \partial Z_L^\alpha}.\end{aligned}\quad (24)$$

We introduce the complex field at each lattice site $a_L(t) \equiv \frac{1}{\sqrt{2\lambda}} [u_L^X(t) + iu_L^P(t)]$, where $\lambda = \hbar k^2 / m\omega_{ax}$ is the dimensionless Planck constant, and obtain the Hamiltonian from Eq. (19)

$$\mathcal{H}/\lambda = \sum_{L,L'} h_{LL'} a_L^\dagger a_{L'} + \frac{1}{2} g_{LL'} a_L^\dagger a_{L'}^\dagger + \frac{1}{2} g_{L'L}^* a_L a_{L'} \quad (25)$$

Here, h_{LL} represents the onsite energy of one excitation on L -th lattice site, $h_{LL'} (L \neq L')$ represents the hopping coefficient from L' -th lattice site to L -th lattice site, and $g_{LL'}$ represents pairing coefficient of creating or annihilating two phase-space phonons on the L -th and L' -th lattice sites. These coefficients are given by the phase space force matrix

$$\begin{cases} h_{LL'} \equiv \frac{1}{2} (\eta_{XX}^{LL'} + \eta_{PP}^{LL'}) + i\frac{1}{2} (\eta_{PX}^{LL'} - \eta_{XP}^{LL'}) \\ g_{LL'} \equiv \frac{1}{2} (\eta_{XX}^{LL'} - \eta_{PP}^{LL'}) + i\frac{1}{2} (\eta_{PX}^{LL'} + \eta_{XP}^{LL'}). \end{cases} \quad (26)$$

From the property $\eta_{\alpha\beta}^{LL'} = \eta_{\beta\alpha}^{L'L}$, we have $h_{LL'} = h_{L'L}^*$ and $g_{LL'} = g_{L'L}$.

Below, we calculate the explicit form of $h_{LL'}$ and $g_{LL'}$ for the case of Coulomb-type interaction $U(R_{LL'}) = \gamma\pi^{-1} R_{LL'}^{-1}$. For the off-site ($L \neq L'$) coefficients, we have the hopping coefficients

$$\begin{aligned}h_{LL'} &= -\frac{U'(R_{LL'})}{R_{LL'}} - \frac{1}{2} \frac{U''(R_{LL'}) R_{LL'} - U'(R_{LL'})}{R_{LL'}^3} \\ &= -\frac{1}{2} \frac{U''(R_{LL'}) R_{LL'} + U'(R_{LL'})}{R_{LL'}^3} \\ &= -\frac{\gamma}{2\pi R_{LL'}^3}\end{aligned}\quad (27)$$

and the pairing coefficients

$$\begin{aligned}g_{LL'} &= -\frac{1}{2} \frac{U''(R_{LL'}) R_{LL'} - U'(R_{LL'})}{R_{LL'}^3} \left[(X_L - X_{L'})^2 - (P_L - P_{L'})^2 + i2(X_L - X_{L'})(P_L - P_{L'}) \right] \\ &= -\frac{1}{2} \frac{U''(R_{LL'}) R_{LL'} - U'(R_{LL'})}{R_{LL'}^3} e^{i2\varphi_{LL'}} \\ &= -\frac{3\gamma}{2\pi R_{LL'}^3} e^{i2\varphi_{LL'}},\end{aligned}\quad (28)$$

where the phase parameter $\varphi_{LL'}$ is defined via

$$X_L - X_{L'} = R_{LL'} \cos \varphi_{LL'}, \quad P_L - P_{L'} = R_{LL'} \sin \varphi_{LL'}. \quad (29)$$

For the on-site ($L = L'$) coefficients, we have the on-site energy

$$\begin{aligned}
\omega_L \equiv h_{LL} &= \frac{1}{2}(T_{XX}^{LL} + T_{PP}^{LL}) - \frac{1}{2} \sum_{L' \neq L} (\Phi_{XX}^{LL'} + \Phi_{PP}^{LL'}) \\
&= \frac{1}{2}(T_{XX}^{LL} + T_{PP}^{LL}) + \frac{1}{2} \sum_{L' \neq L} \frac{U''(R_{LL'})R_{LL'} + U'(R_{LL'})}{R_{LL'}} \\
&= \frac{1}{2}(T_{XX}^{LL} + T_{PP}^{LL}) + \sum_{L' \neq L} \frac{\gamma}{2\pi R_{LL'}^3}.
\end{aligned} \tag{30}$$

and the squeezing rates

$$g_L \equiv g_{LL} = \frac{1}{2}(T_{XX}^{LL} - T_{PP}^{LL}) + iT_{PX}^{LL} + \sum_{L' \neq L} \frac{3\gamma}{2\pi R_{LL'}^3} e^{i2\varphi_{LL'}}. \tag{31}$$

The above expressions are valid for any boundary condition and arbitrary single-particle Hamiltonian. Finally, we obtain the Hamiltonian of phase-space lattice waves

$$\frac{\mathcal{H}}{\lambda} = \sum_L \omega_L a_L^\dagger a_L + \frac{1}{2} g_L a_L^{\dagger 2} + \frac{1}{2} g_L^* a_L^2 - \frac{\gamma}{4\pi} \left(\sum_{L \neq L'} \frac{a_L^\dagger a_{L'} + 3e^{i2\varphi_{LL'}} a_L^\dagger a_{L'}^\dagger}{|\mathbf{Z}_L^0 - \mathbf{Z}_{L'}^0|^3} + h.c. \right). \tag{32}$$

For the honeycomb single-particle Hamiltonian (11) and periodic boundary conditions, we have the simplified results of on-site coefficients

$$\omega_L = \omega_0 \pm 2\Delta + \sum_{L' \neq L} \frac{\gamma}{2\pi R_{LL'}^3}, \quad g_L = 0, \tag{33}$$

where the summation in Eq. (31) disappears due to the honeycomb lattice symmetry. The Hamiltonian Eq. (32) describes phonons propagating in our honeycomb phase-space crystal. It is reminiscent of the tight-binding model for electrons in graphene but our phase-space phonons can hop between any two arbitrarily distant sites reflecting the long-range nature of the atom-atom interaction.

Pairing-induced staggered magnetic field

In order to better distinguish the effects of the (long-range) hopping and the pairing interaction, it is instructive to first consider a regime where the latter is suppressed, i.e., the creation of phonon pairs is far off-resonant $|\gamma| \ll |\omega_0|$. In this case, we can cancel the pairing-interaction terms in the Hamiltonian (25) using the following unitary transformation

$$U \equiv \exp \left(\sum_{\bar{L}, \bar{L}'} \xi_{\bar{L}\bar{L}'} a_{\bar{L}}^\dagger a_{\bar{L}'}^\dagger - \xi_{\bar{L}'\bar{L}}^* a_{\bar{L}} a_{\bar{L}'} \right) \equiv e^Y. \tag{34}$$

It can be checked that $U^\dagger = e^{-Y}$ and thus $U^\dagger U = 1$. Using the following identities

$$\begin{aligned}
[a_L^\dagger a_{L'}, a_{\bar{L}}^\dagger a_{\bar{L}'}^\dagger] &= a_L^\dagger a_{\bar{L}}^\dagger \delta_{L'\bar{L}} + a_L^\dagger a_{\bar{L}}^\dagger \delta_{L'\bar{L}'} \\
[a_L^\dagger a_{L'}, a_{\bar{L}} a_{\bar{L}'}] &= -a_{\bar{L}'} a_{L'} \delta_{L\bar{L}} - a_{\bar{L}} a_{L'} \delta_{L\bar{L}'} \\
[a_L^\dagger a_{L'}, a_{\bar{L}}^\dagger a_{\bar{L}'}] &= -a_L^\dagger a_{\bar{L}} \delta_{L'\bar{L}} - a_L^\dagger a_{\bar{L}} \delta_{L'\bar{L}'} - a_{\bar{L}'} a_L^\dagger \delta_{L\bar{L}} - a_{\bar{L}} a_L^\dagger \delta_{L\bar{L}'} \\
[a_L a_{L'}, a_{\bar{L}}^\dagger a_{\bar{L}'}^\dagger] &= a_L a_{\bar{L}}^\dagger \delta_{L'\bar{L}'} + a_L a_{\bar{L}}^\dagger \delta_{L'\bar{L}} + a_{\bar{L}'} a_L^\dagger \delta_{L\bar{L}} + a_{\bar{L}} a_L^\dagger \delta_{L\bar{L}'},
\end{aligned} \tag{35}$$

we obtain

$$\begin{aligned}
[a_L^\dagger a_{L'}, Y] &= \sum_{\bar{L}} \tilde{\xi}_{\bar{L}L'} a_L^\dagger a_{\bar{L}}^\dagger + \tilde{\xi}_{\bar{L}L}^* a_{\bar{L}} a_{L'}, \\
[a_L^\dagger a_{L'}, Y] &= \sum_{\bar{L}} \tilde{\xi}_{\bar{L}L'}^* a_L^\dagger a_{\bar{L}} + \tilde{\xi}_{\bar{L}L} a_{\bar{L}} a_L^\dagger, \\
[a_L a_{L'}, Y] &= \sum_{\bar{L}} \tilde{\xi}_{\bar{L}L'} a_L a_{\bar{L}}^\dagger + \tilde{\xi}_{\bar{L}L} a_L^\dagger a_{\bar{L}},
\end{aligned} \tag{36}$$

where we have defined $\tilde{\xi}_{LL'} \equiv \xi_{LL'} + \xi_{L'\bar{L}}$ with $\tilde{\xi}_{LL'} = \tilde{\xi}_{L'\bar{L}}$. The Hamiltonian transformed by U to the leading order

$$U^\dagger \mathcal{H} U / \lambda = \mathcal{H} / \lambda + [\mathcal{H} / \lambda, Y] + \dots \quad (37)$$

where we have used the Hausdorff expansion

$$e^{-Y} \mathcal{H} e^Y = \mathcal{H} + [\mathcal{H}, Y] + \frac{1}{2!} [[\mathcal{H}, Y], Y] + \dots$$

The leading-order correction is

$$\begin{aligned} [\mathcal{H} / \lambda, Y] &= \sum_{L; L'; \bar{L}} h_{LL'} \xi_{\bar{L}L'} a_{Ls}^\dagger a_{L'}^\dagger + h_{LL'} \xi_{LL}^* a_{\bar{L}} a_{L'} \\ &\quad + \frac{1}{2} g_{LL'} \tilde{\xi}_{\bar{L}L'}^* a_L^\dagger a_{\bar{L}} + \frac{1}{2} g_{LL'} \tilde{\xi}_{LL}^* a_{\bar{L}} a_{L'}^\dagger + \frac{1}{2} g_{L'L}^* \tilde{\xi}_{LL'} a_L a_L^\dagger + \frac{1}{2} g_{L'L}^* \tilde{\xi}_{LL} a_L^\dagger a_{L'} \\ &= \sum_{L; L'} \tilde{h}_{LL'} a_L^\dagger a_{L'} + \frac{1}{2} \tilde{g}_{LL'} a_L^\dagger a_{L'}^\dagger + \frac{1}{2} \tilde{g}_{L'L}^* a_L a_{L'}^\dagger. \end{aligned} \quad (38)$$

Neglecting constants from $a_L a_L^\dagger = a_L^\dagger a_L + 1$ and using the symmetry property $g_{LL'} = g_{L'L}$, we have the coefficients

$$\tilde{h}_{LL'} = \sum_{\bar{L}} g_{\bar{L}L'}^* \tilde{\xi}_{\bar{L}L} + g_{L\bar{L}} \tilde{\xi}_{LL'}^*, \quad \tilde{g}_{LL'} = \sum_{\bar{L}} h_{L\bar{L}} \tilde{\xi}_{\bar{L}L'}, \quad \tilde{g}_{L'L}^* = \sum_{\bar{L}} h_{\bar{L}L'} \tilde{\xi}_{\bar{L}L}^*. \quad (39)$$

To cancel the pairing terms in the Hamiltonian (25), it needs $g_{LL'} + \tilde{g}_{LL'} = 0$, i.e.,

$$g_{LL'} = - \sum_{\bar{L}} h_{L\bar{L}} \tilde{\xi}_{\bar{L}L'}. \quad (40)$$

We make the assumption that the on-site energy is much larger than the off-site hopping terms, i.e., $\omega_L \equiv h_{LL} \gg h_{L\bar{L}}$ with $L \neq \bar{L}$, which results in

$$\tilde{\xi}_{LL'} \approx - \frac{g_{LL'}}{\omega_L} \implies \xi_{LL'} = \xi_{L'L} = - \frac{g_{LL'}}{2\omega_L}.$$

Finally, we have the pairing-induced hopping rate

$$\tilde{h}_{LL'} \approx - \sum_{\bar{L}} \frac{2}{\omega_{\bar{L}}} g_{L\bar{L}} g_{\bar{L}L'}^*. \quad (41)$$

Note that the pairing-induced hopping is proportional to the square of interaction strength $|\tilde{h}_{L\bar{L}}| \propto \gamma^2 / \omega_0$. Considering the case beyond NN interaction, there is a direct real-valued hopping rate between lattice sites L and \bar{L} , which is proportional to the interaction strength $h_{L\bar{L}} \propto \gamma$. As a result, the pairing-induced non-reciprocal hopping pathway $\tilde{h}_{L\bar{L}}$ interferes with a direct hopping pathway $h_{L\bar{L}}$ leads to a weak staggered magnetic flux of the order $\Phi \sim \gamma / \omega_0$. This is the essential ingredients of Haldane model [3], which introduces a staggered magnetic field breaking the time-reversal symmetry inside each unit cell but leaving the total net flux through the unit cell zero.

Our model recovers the anomalous quantum Hall effect similar to the Haldane model only in the weak off-resonant interaction regime. Our effective particle-conserving description (which is derived from a perturbation theory in γ / ω_0) differs from the Haldane model in that it includes long-range hopping transitions. For sufficiently strong interaction (non-perturbative regime), our model has some new features which do not appear in Haldane model, e.g., new topological phase regime and the loss of stability.

III. Topological band structures

Periodic boundary condition

For periodic boundaries both in X and P directions, we Fourier transform the linearised Hamiltonian (25) using

$$a_{l,s} = \frac{1}{\sqrt{N}} \sum_{\mathbf{k}} a_{\mathbf{k},s} \exp(i\mathbf{k} \cdot \mathbf{Z}_{l,s}^0); \quad a_{l,s}^\dagger = \frac{1}{\sqrt{N}} \sum_{\mathbf{k}} a_{\mathbf{k},s}^\dagger \exp(-i\mathbf{k} \cdot \mathbf{Z}_{l,s}^0), \quad (42)$$

where $\mathbf{k} = (k_X, k_P)$, $Z_{l,s}^0$ is the equilibrium position of atom $L = (l, s)$ and N is the total number of unite cells. The operators from inverse Fourier transformation

$$a_{\mathbf{k},s} = \frac{1}{\sqrt{N}} \sum_l a_{l,s} \exp(-i\mathbf{k} \cdot \mathbf{Z}_{l,s}^0); \quad a_{\mathbf{k},s}^\dagger = \frac{1}{\sqrt{N}} \sum_l a_{l,s}^\dagger \exp(i\mathbf{k} \cdot \mathbf{Z}_{l,s}^0), \quad (43)$$

satisfy the commutation of Bosons, i.e.,

$$[a_{\mathbf{k},s}, a_{\mathbf{k}',s'}^\dagger] = \delta_{\mathbf{k}\mathbf{k}'} \delta_{ss'}; \quad [a_{\mathbf{k},s}, a_{\mathbf{k}',s'}] = 0. \quad (44)$$

The hopping terms in the Hamiltonian (25) become

$$\begin{aligned} \sum_{l,l'} h_{(l,s),(l',s')} a_{l,s}^\dagger a_{l',s'} &= \frac{1}{N} \sum_{\mathbf{k},\mathbf{k}'} a_{\mathbf{k},s}^\dagger a_{\mathbf{k}',s'} \sum_{l,l'} h_{(l,s),(l',s')} e^{-i\mathbf{k} \cdot (\mathbf{Z}_{l,s}^0 - \mathbf{Z}_{l',s'}^0) - i(\mathbf{k} - \mathbf{k}') \cdot \mathbf{Z}_{l',s'}^0} \\ &\equiv \sum_{\mathbf{k}} h_{s,s'}(\mathbf{k}) a_{\mathbf{k},s}^\dagger a_{\mathbf{k},s'} \end{aligned} \quad (45)$$

with the definition of hopping coefficients in reciprocal $\mathbf{k} = (k_X, k_P)$ space

$$h_{s,s'}(\mathbf{k}) \equiv \sum_l h_{(l,s),(l',s')} \exp[-i\mathbf{k} \cdot (\mathbf{Z}_{l,s}^0 - \mathbf{Z}_{l',s'}^0)]. \quad (46)$$

We find the property $h_{s',s}^*(\mathbf{k}) = h_{s',s}(\mathbf{k})$ using the identity $h_{(l,s),(l',s')} = h_{(l',s'),(l,s)}^*$ and the discrete translational lattice symmetry. Similarly, the pairing terms in the Hamiltonian (25) become

$$\begin{aligned} \sum_{l,l'} g_{(l,s),(l',s')} a_{l,s}^\dagger a_{l',s'}^\dagger &= \frac{1}{N} \sum_{\mathbf{k},\mathbf{k}'} a_{\mathbf{k},s}^\dagger a_{\mathbf{k}',s'}^\dagger \sum_{l,l'} g_{(l,s),(l',s')} e^{-i\mathbf{k} \cdot (\mathbf{Z}_{l,s}^0 - \mathbf{Z}_{l',s'}^0) - i(\mathbf{k} + \mathbf{k}') \cdot \mathbf{Z}_{l',s'}^0} \\ &= \sum_{\mathbf{k}} g_{s,s'}(\mathbf{k}) a_{\mathbf{k},s}^\dagger a_{-\mathbf{k},s'}^\dagger \end{aligned} \quad (47)$$

with the definition of pairing coefficient in reciprocal $\mathbf{k} = (k_X, k_P)$ space

$$g_{s,s'}(\mathbf{k}) \equiv \sum_l g_{(l,s),(l',s')} \exp[-i\mathbf{k} \cdot (\mathbf{Z}_{l,s}^0 - \mathbf{Z}_{l',s'}^0)]. \quad (48)$$

We find the property $g_{s,s'}(-\mathbf{k}) = g_{s',s}(\mathbf{k})$ using the identity $g_{(l,s),(l',s')} = g_{(l',s'),(l,s)}$ and the discrete lattice translational symmetry. As a result, the Hamiltonian in the reciprocal space is given by

$$\begin{aligned} \mathcal{H}/\lambda &= \sum_{\mathbf{k},s,s'} h_{s,s'}(\mathbf{k}) a_{\mathbf{k},s}^\dagger a_{\mathbf{k},s'} + \frac{1}{2} g_{s,s'}(\mathbf{k}) a_{\mathbf{k},s}^\dagger a_{-\mathbf{k},s'}^\dagger + \frac{1}{2} g_{s',s}^*(\mathbf{k}) a_{-\mathbf{k},s'} a_{\mathbf{k},s} \\ &= \sum_{\mathbf{k}} \mathbf{A}_{\mathbf{k}}^T \mathcal{H}_{\mathbf{k}} \mathbf{A}_{\mathbf{k}}, \end{aligned} \quad (49)$$

where we have deined the vector $\mathbf{A}_{\mathbf{k}} \equiv (a_{\mathbf{k},A}, a_{\mathbf{k},B}, a_{-\mathbf{k},A}^\dagger, a_{-\mathbf{k},B}^\dagger)^T$ and the Bogoliubov-de-Gennes (BdG) Hamiltonian

$$\mathcal{H}_{\mathbf{k}} \equiv \begin{pmatrix} h_{A,A}(\mathbf{k}) & h_{A,B}(\mathbf{k}) & \frac{1}{2}g_{A,A}(\mathbf{k}) & \frac{1}{2}g_{A,B}(\mathbf{k}) \\ h_{B,A}(\mathbf{k}) & h_{B,B}(\mathbf{k}) & \frac{1}{2}g_{B,A}(\mathbf{k}) & \frac{1}{2}g_{B,B}(\mathbf{k}) \\ \frac{1}{2}g_{A,A}^*(\mathbf{k}) & \frac{1}{2}g_{A,B}^*(\mathbf{k}) & h_{A,A}(-\mathbf{k}) & h_{A,B}(-\mathbf{k}) \\ \frac{1}{2}g_{B,A}^*(\mathbf{k}) & \frac{1}{2}g_{B,B}^*(\mathbf{k}) & h_{B,A}(-\mathbf{k}) & h_{B,B}(-\mathbf{k}) \end{pmatrix}. \quad (50)$$

From the Heisenberg equation

$$-i \frac{d}{dt} a_{\mathbf{k},s} = \frac{1}{\lambda} [\mathcal{H}, a_{\mathbf{k},s}] = \sum_{s'} -h_{s,s'}(\mathbf{k}) a_{\mathbf{k},s'} - \frac{1}{2} g_{s,s'}(\mathbf{k}) a_{-\mathbf{k},s'}^\dagger - \frac{1}{2} g_{s',s}(-\mathbf{k}) a_{-\mathbf{k},s'}^\dagger,$$

we have the EOM for the ladder operator $\mathbf{A}_{\mathbf{k}}$ as following

$$i \frac{d}{dt} \mathbf{A}_{\mathbf{k}} = D(\mathbf{k}) \mathbf{A}_{\mathbf{k}}. \quad (51)$$

Here $D(\mathbf{k})$ is the dynamical matrix defined by

$$D(\mathbf{k}) \equiv \begin{pmatrix} h_{A,A}(\mathbf{k}) & h_{A,B}(\mathbf{k}) & \bar{g}_{A,A}(\mathbf{k}) & \bar{g}_{A,B}(\mathbf{k}) \\ h_{B,A}(\mathbf{k}) & h_{B,B}(\mathbf{k}) & \bar{g}_{B,A}(\mathbf{k}) & \bar{g}_{B,B}(\mathbf{k}) \\ -\bar{g}_{A,A}^*(\mathbf{k}) & -\bar{g}_{B,A}^*(\mathbf{k}) & -h_{A,A}^*(-\mathbf{k}) & -h_{A,B}^*(-\mathbf{k}) \\ -\bar{g}_{A,B}^*(\mathbf{k}) & -\bar{g}_{B,B}^*(\mathbf{k}) & -h_{B,A}^*(-\mathbf{k}) & -h_{B,B}^*(-\mathbf{k}) \end{pmatrix} \quad (52)$$

with the symmetric pairing coefficients defined by

$$\bar{g}_{s,s'}(\mathbf{k}) \equiv \frac{1}{2} [g_{s,s'}(\mathbf{k}) + g_{s',s}(-\mathbf{k})].$$

The eigen solutions of EOM (51) can be obtained by diagonalising the dynamical matrix $D(\mathbf{k})$. We label the frequency spectrum by $\omega_{\mathbf{k},n}$, where $n = 1, 2, 3, 4$ is the index of four bands. For each given \mathbf{k} and band index n , the eigenstate is a four-component vector $|\mathbf{k}, n\rangle = (u_{n,A}, u_{n,B}, v_{n,A}, v_{n,B})$. Then, the Hamiltonian can be cast into a diagonal form of

$$\mathcal{H}/\lambda = \sum_{\mathbf{k},n} \omega_{\mathbf{k},n} b_{\mathbf{k},n}^\dagger b_{\mathbf{k},n}, \quad (53)$$

where the normal modes are given by a Bogoliubov transformation in the form of

$$b_{\mathbf{k},n}^\dagger = \sum_{s=A,B} u_{n,s}(\mathbf{k}) a_{\mathbf{k},s}^\dagger + v_{n,s}(\mathbf{k}) a_{-\mathbf{k},s}.$$

From the property $\bar{g}_{s,s'}(\mathbf{k}) = \bar{g}_{s,s'}(-\mathbf{k})$, the dynamical matrix has *particle-hole symmetry* expressed by

$$\Xi D(\mathbf{k}) \Xi^{-1} = -D(-\mathbf{k}). \quad (54)$$

The particle-hole operator is defined via $\Xi = \tau_x K$ satisfies $\Xi^2 = +1$, where

$$\tau_x = \begin{pmatrix} 0 & 0 & 1 & 0 \\ 0 & 0 & 0 & 1 \\ 1 & 0 & 0 & 0 \\ 0 & 1 & 0 & 0 \end{pmatrix} \quad (55)$$

and K is the complex conjugation. It follows that each eigenmode at frequency $\omega(\mathbf{k})$ has a partner eigenmode at $-\omega(-\mathbf{k})$, namely, creating a quasiparticle in the state $\omega(\mathbf{k})$ has the same effect as removing one (creating a hole) from the state $-\omega(-\mathbf{k})$. Therefore, we label the two upper bands ($n = 1, 2$) as particle bands and two lower bands ($n = 3, 4$) as the hole bands. From the bosonic commutation relationship $[b_{\mathbf{k}',n'}, b_{\mathbf{k},n}^\dagger] = \delta_{n,n'} \delta_{\mathbf{k}',\mathbf{k}}$, the eigenmodes have to follow the ortho-normal condition

$$\langle \mathbf{k}, n' | \Sigma_z | \mathbf{k}, n \rangle \equiv \sum_s u_{n',s}^* u_{n,s} - v_{n',s}^* v_{n,s} = \pm \delta_{n,n'}, \quad (56)$$

where $\Sigma_z \equiv \text{diag}(1, 1, -1, -1)$ is a 4×4 diagonal matrix and the positive (negative) sign corresponds to particle (hole) bands.

Symplectic Chern number

Different from the particle-conserving case, the ground state of the BdG Hamiltonian $\mathcal{H}_{\mathbf{k}}$ is a multi-mode squeezed state with non-zero phonon/photon number. By regarding the $\mathbf{k} = (k_X, k_P)$ as an external adiabatic parameter, we calculate the Berry phase accumulated by a single Bogoliubov quasi-particle in a specific n -th band along a closed loop covering the whole Brillouin zone (BZ), i.e.,

$$\begin{aligned} \Phi_n &= i \oint_{BZ} \langle S_{\mathbf{k}} | b_{\mathbf{k},n} \nabla_{\mathbf{k}} b_{\mathbf{k},n}^\dagger | S_{\mathbf{k}} \rangle \cdot d\mathbf{k} \\ &= i \oint_{BZ} \langle S_{\mathbf{k}} | [b_{\mathbf{k},n} \nabla_{\mathbf{k}} b_{\mathbf{k},n}^\dagger] | S_{\mathbf{k}} \rangle \cdot d\mathbf{k} + i \oint_{BZ} \langle S_{\mathbf{k}} | \nabla_{\mathbf{k}} | S_{\mathbf{k}} \rangle \cdot d\mathbf{k} \\ &= i \oint_{BZ} \left[\sum_s u_{n,s}^*(\mathbf{k}) \nabla_{\mathbf{k}} u_{n,s}(\mathbf{k}) - v_{n,s}^*(\mathbf{k}) \nabla_{\mathbf{k}} v_{n,s}(\mathbf{k}) \right] \cdot \mathbf{k} + i \oint_{BZ} \langle S_{\mathbf{k}} | \nabla_{\mathbf{k}} | S_{\mathbf{k}} \rangle \cdot d\mathbf{k} \\ &\equiv \oint_{BZ} \mathcal{A}_n(\mathbf{k}) \cdot \mathbf{k} + \phi_n. \end{aligned} \quad (57)$$

Here, $|S_{\mathbf{k}}\rangle$ is the ground state (Bogoliubov vacuum state) of $\mathcal{H}_{\mathbf{k}}$ and, in the second line, we have used $b_{\mathbf{k},n}|S_{\mathbf{k}}\rangle = 0$ by the definition of vacuum state. Because of the unusual ortho-normalization (56), we have updated the definition of the Berry connection by [8, 40]

$$\mathcal{A}_n(\mathbf{k}) = i\langle \mathbf{k}, n | \Sigma_z \nabla_{\mathbf{k}} | \mathbf{k}, n \rangle. \quad (58)$$

Note that the Berry connection defined here for the Bosonic many-body second-quantized Hamiltonian is different from the Berry connection for the single-particle Hamiltonian. The Bogoliubov vacuum $|S_{\mathbf{k}}\rangle$ depends on \mathbf{k} and could possibly accumulate a Berry phase, i.e., $\oint \langle S_{\mathbf{k}} | \nabla_{\mathbf{k}} | S_{\mathbf{k}} \rangle \cdot d\mathbf{k} \neq 0$. However, the Berry phase of our interest is the additional Berry phase accumulated by the quasi-particle, i.e., the difference of Bogoliubov vacuum Berry phase and that associated with a single quasiparticle excitation. We thus update the definition of Chern number by [8, 40]

$$C_n = \frac{1}{2\pi} \int_{BZ} (\nabla_{\mathbf{k}} \times \mathcal{A}_n(\mathbf{k})) \cdot \hat{\mathbf{n}} \in \mathbb{Z}, \quad (59)$$

where $\hat{\mathbf{n}}$ is the unit vector normal to the \mathbf{k} -plane. Due to the additional element Σ_z in the Berry connection (58), the quantity given by Eq. (59) is also called *symplectic Chern number*. Since the quantum states come back to itself along a closed loop, the quantities Φ_n and ϕ_n are integers multiple of 2π , and thus the symplectic Chern number is also an integer.

As there is no net geometric phase (total flux of synthetic magnetic field) in our model, the sum of the Chern numbers over the particle bands must be zero. The Chern number of individual band may change after a phase transition where two or more bands touch each other, but their sum does not change. For this reason, we define the Chern number of the lowest band as the Chern number of our system $C = C_1$.

Strip boundary condition

For the periodic boundary in X direction but open boundary in P direction (strip boundary condition), we can only perform Fourier transformation in X direction

$$a_{l,s} = \frac{1}{\sqrt{N_X}} \sum_{k_X} a_{k_X, (l_P, s)} \exp(ik_X X_{l,s}^0); \quad a_{l,s}^\dagger = \frac{1}{\sqrt{N_X}} \sum_{k_X} a_{k_X, (l_P, s)}^\dagger \exp(-ik_X X_{l,s}^0), \quad (60)$$

where N_X is the number of unit cells in X direction and (l_P, s) labels the position of atoms in P direction. Then, the hopping terms in the Hamiltonian (25) become

$$\begin{aligned} \sum_{l,l'} h_{(l,s), (l',s')} a_{l,s}^\dagger a_{l',s'} &= \frac{1}{N_X} \sum_{l,l'} \sum_{k_X, k'_X} a_{k_X, (l_P, s)}^\dagger a_{k'_X, (l'_P, s')} h_{(l,s), (l',s')} e^{-ik_X (X_{l,s}^0 - X_{l',s'}^0) - i(k_X - k'_X) X_{l',s'}^0} \\ &= \sum_{l_P, l'_P} \sum_{k_X} h_{(l_P, s), (l'_P, s')}(k_X) a_{k_X, (l_P, s)}^\dagger a_{k_X, (l'_P, s')} \end{aligned} \quad (61)$$

with the Fourier transformation of hopping coefficients

$$h_{(l_P, s), (l'_P, s')}(k_X) \equiv \sum_{l_X} h_{(l,s), (l',s')} \exp[-ik_X \cdot (X_{l,s}^0 - X_{l',s'}^0)], \quad (62)$$

which has the property $h_{(l'_P, s'), (l_P, s)}^*(k_X) = h_{(l_P, s), (l'_P, s')}(k_X)$ using the identity $h_{(l,s), (l',s')} = h_{(l',s'), (l,s)}^*$ and discrete translational symmetry in X -direction. Similarly, the pairing terms in the Hamiltonian (25) become

$$\begin{aligned} \sum_{l,l'} g_{s,s'}(l-l') a_{l,s}^\dagger a_{l',s'}^\dagger &= \frac{1}{N_X} \sum_{l,l'} \sum_{k_X, k'_X} a_{k_X, (l_P, s)}^\dagger a_{k'_X, (l'_P, s')}^\dagger g_{(l,s), (l',s')} e^{-ik_X (X_{l,s}^0 - X_{l',s'}^0) - i(k_X + k'_X) X_{l',s'}^0} \\ &= \sum_{l_P, l'_P} \sum_{k_X} g_{(l_P, s), (l'_P, s')}(k_X) a_{k_X, (l_P, s)}^\dagger a_{-k_X, (l'_P, s')}^\dagger \end{aligned} \quad (63)$$

with the Fourier transformation of pairing coefficients

$$g_{(l_P, s), (l'_P, s')}(k_X) \equiv \sum_{l_X} g_{(l,s), (l',s')}(l-l') \exp[-ik_X \cdot (X_{l,s}^0 - X_{l',s'}^0)], \quad (64)$$

which has the property of $g_{(l_P,s),(l'_P,s')}(-k_X) = g_{(l'_P,s'),(l_P,s)}(k_X)$ using the identity $g_{(l,s),(l',s')} = g_{(l',s'),(l,s)}$ and discrete translational symmetry in X -direction. Therefore, the Hamiltonian in momentum space is

$$\begin{aligned} \mathcal{H}/\lambda = & \sum_{l_P,l'_P} \sum_{k_X} h_{(l_P,s),(l'_P,s')}(k_X) a_{k_X,(l_P,s)}^\dagger a_{k_X,(l'_P,s')} \\ & + \frac{1}{2} g_{(l_P,s),(l'_P,s')}(k_X) a_{k_X,(l_P,s)}^\dagger a_{-k_X,(l'_P,s')}^\dagger + \frac{1}{2} g_{(l_P,s),(l'_P,s')}^*(k_X) a_{k_X,(l_P,s)} a_{-k_X,(l'_P,s')} \end{aligned}$$

From the Heisenberg equation

$$\begin{aligned} -i \frac{d}{dt} a_{k_X,(l_P,s)} = & \sum_{l'_P,s'} -h_{(l_P,s),(l'_P,s')}(k_X) a_{k_X,(l'_P,s')} \\ & - \frac{1}{2} [g_{(l_P,s),(l'_P,s')}(k_X) + g_{(l'_P,s'),(l_P,s)}(-k_X)] a_{-k_X,(l'_P,s')}^\dagger, \end{aligned} \quad (65)$$

we have EOM for the operator $\mathbf{A}_{l_P}(k_X) \equiv (a_{k_X,(l_P,A)}, a_{k_X,(l_P,B)}, a_{-k_X,(l_P,A)}^\dagger, a_{-k_X,(l_P,B)}^\dagger)^T$

$$i \frac{d}{dt} \begin{pmatrix} \mathbf{A}_1 \\ \vdots \\ \mathbf{A}_{l'_P} \\ \vdots \\ \mathbf{A}_{N_P} \end{pmatrix} = \begin{pmatrix} D_{(l_P=1,l'_P=1)} & \cdots & D_{(l_P=1,l'_P)} & \cdots & D_{(l_P=1,l'_P=N_P)} \\ \vdots & \ddots & \vdots & \vdots & \vdots \\ D_{(l_P,l'_P=1)} & \cdots & D_{l'_P,l_P} & \cdots & D_{(l_P,l'_P=N_P)} \\ \vdots & \vdots & \vdots & \ddots & \vdots \\ D_{(l_P=N_P,l'_P=1)} & \cdots & D_{(l_P=N_P,l'_P)} & \cdots & D_{(l_P=N_P,l'_P=N_P)} \end{pmatrix} \begin{pmatrix} \mathbf{A}_1 \\ \vdots \\ \mathbf{A}_{l'_P} \\ \vdots \\ \mathbf{A}_{N_P} \end{pmatrix},$$

where the block matrix element is given by

$$D_{(l_P,l'_P)}(k_X) \equiv \begin{pmatrix} h_{(l_P,A),(l'_P,A)}(k_X) & h_{(l_P,A),(l'_P,B)}(k_X) & \bar{g}_{(l_P,A),(l'_P,A)}(k_X) & \bar{g}_{(l_P,A),(l'_P,B)}(k_X) \\ h_{(l_P,B),(l'_P,A)}(k_X) & h_{(l_P,B),(l'_P,B)}(k_X) & \bar{g}_{(l_P,B),(l'_P,A)}(k_X) & \bar{g}_{(l_P,B),(l'_P,B)}(k_X) \\ -\bar{g}_{(l_P,A),(l'_P,A)}^*(-k_X) & -\bar{g}_{(l_P,A),(l'_P,B)}^*(-k_X) & -h_{(l_P,A),(l'_P,A)}^*(-k_X) & -h_{(l_P,A),(l'_P,B)}^*(-k_X) \\ -\bar{g}_{(l_P,B),(l'_P,A)}^*(-k_X) & -\bar{g}_{(l_P,B),(l'_P,B)}^*(-k_X) & -h_{(l_P,B),(l'_P,A)}^*(-k_X) & -h_{(l_P,B),(l'_P,B)}^*(-k_X) \end{pmatrix}$$

with the modified pairing coefficient

$$\bar{g}_{(l_P,s),(l'_P,s')}(k_X) \equiv \frac{1}{2} [g_{(l_P,s),(l'_P,s')}(k_X) + g_{(l'_P,s'),(l_P,s)}(-k_X)]. \quad (66)$$

By extending the definition of operator τ_x in Eq. (55) to all the matrix elements of $D(k_X)$ labelled by (l_P, l'_P) and using the property $\bar{g}_{(l_P,s),(l'_P,s')}(k_X) = \bar{g}_{(l_P,s),(l'_P,s')}(-k_X)$, the dynamical matrix $D_{(l_P,l'_P)}(k_X)$ has *particle-hole symmetry* expressed by

$$\Xi D_{(l_P,l'_P)}(k_X) \Xi^{-1} = -D_{(l_P,l'_P)}(-k_X), \quad (67)$$

where the particle-hole operator is defined via $\Xi = \tau_x K$ satisfies $\Xi^2 = +1$. Again, we should diagonalise the dynamical matrix $D(k_X)$, instead of the Hamiltonian, to solve EOM and obtain the eigenmodes.

Chirality of topological edge states

In Fig. 6, we show the band structures of strip phase-space crystal in different parameter regimes of corresponding bulk topological phase diagram. The three upper plots (from left to right) represent three typical band structures for zero onsite detuning $\Delta = 0$ and different interaction strengths. For $\gamma/\omega_0 = 75$, there is only one chiral topological transport channel (for a fixed energy indicated by the dashed lines in the gap) on the single boundary of strip phase-space crystal, i.e., there is only single crossing point between the dashed line and one topological band (e.g., the blue one). For $\gamma/\omega_0 = -8$, there are three topological transport channels (three different values of k_X) for a fixed energy in the gap. However, one transport channel has an opposite chirality with the other two channels, e.g., the blue topological band has one edge state propagating along positive X direction and two edge states propagating along negative X direction. In the above two cases, the Chern number are both $C = -1$. As a contrast, for $\gamma/\omega = -18.5$,

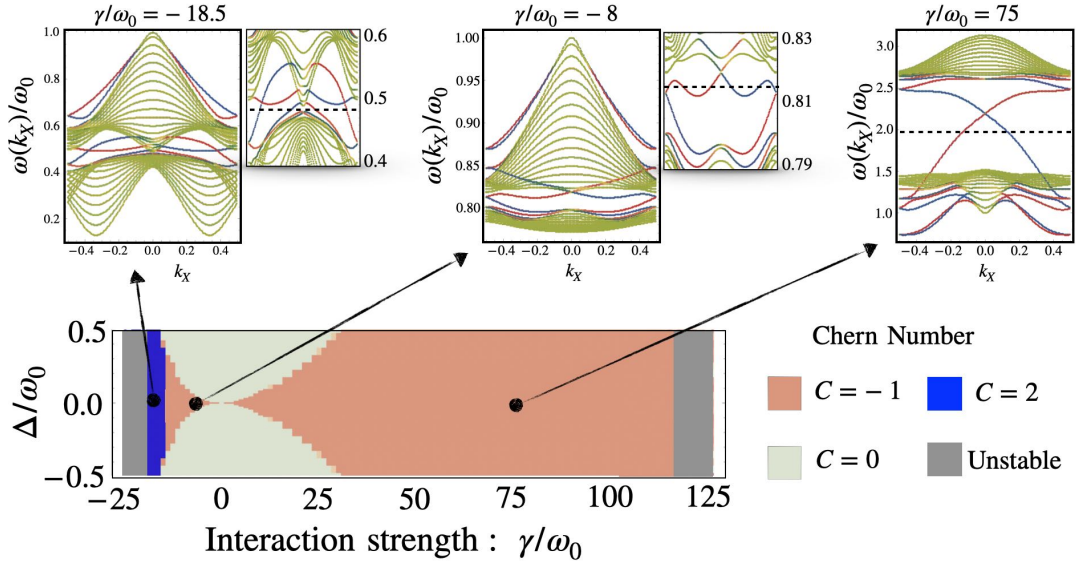


FIG. 6. Band structure of strip phase-space crystals in different topological phases. The three upper plots (from left to right) represent three typical band structures for zero onsite detuning $\Delta = 0$ and three different interaction strengths $\gamma/\omega_0 = -18.5$ ($C = 2$), $\gamma/\omega_0 = -1$ ($C = -1$) and $\gamma/\omega_0 = 75$ ($C = -1$) respectively, where the insets are the zoomed-in band structures around the energy gap. The color on the bands represents the averaged momentum $\langle P \rangle$ of each eigenstate, cf. Fig. 3 of main text. The dashed lines in the band structures are the cutting energies in the gap, whose crossing points with the topological bands indicate the transport channels for a fixed energy. Note that the topological edge states on each single boundary can change their chirality by the interaction, thus transport along the opposite direction.

the Chern number changes its sign and becomes $C = 2$, which means the edge states changes their chirality. For example, the blue topological band has two transport channels both propagating along positive X direction.

The number of topological edge states on one single boundary is concluded by the bulk-boundary correspondence, i.e., the difference between the net number of chiral edge states (counted with a sign depending on their chirality) at two energies is equal to the total Chern number of the intermediate bands. In our model, there are no topological edge states near the zero energy since the particle band cannot touch the hole band for the stable phase space crystals. Therefore, the Chern numbers of bands are sufficient to determine the number of topological edge states [20].

IV. Experiment with cold atoms

Quasi-1D trapping potential

In order to create a quasi-1D harmonic potential for the cold atoms, one can start from a small Bose-Einstein condensate (BEC) in a magnetic trap [54]. Then, the BEC is loaded into a 2D optical potential, along y and z directions as shown by Fig. 1(b) in the main text, by superimposing two orthogonal standing waves on top of the BEC. Each standing wave is formed by two counter-propagating Gaussian laser beams. Supposing the laser light has wavelength (wave vector) λ_L ($k_L = 2\pi/\lambda_L$), the lattice potential has the form of $V(x, y, z) = V_0(\sin^2 ky + \sin^2 kz)$ with the potential depth V_0 laser intensity. As a result, an array of 1D quantum gases confined to narrow potential tubes is created. For a sufficiently strong potential depth (laser intensity), the tunnel coupling and particle exchange between different tubes are exponentially suppressed [32]. The Gaussian profile of the laser beams also leads to axial confinement of the quasi-1D gases. The resulting transverse (in the y - z plane) trapping frequency ω_{tr} and axial trapping frequency ω_{ax} are given by [55]

$$\omega_{tr} = \frac{2E_r}{\hbar} \sqrt{\frac{V_0}{E_r}}, \quad \omega_{ax} = \frac{\lambda_L}{\pi w_0} \omega_{tr}, \quad (68)$$

where $E_r = \hbar^2 k_L^2 / 2m$ is the recoil energy of an atom with mass m , and w_0 is the Gaussian beam waist which sets the length of 1D harmonic trap.

Stroboscopic lattice potential

In our stroboscopic driving scheme, we need to control the stroboscopic lattice constant, which is usually much longer than the wavelength of laser lights. For this purpose, one can superimpose two equally polarized laser beams of wavelength λ_D intersecting at an angle θ as shown by Fig. 1(b) in the main text. The result is a standing wave optical dipole potential with a spatial period of [56]

$$d = \frac{\lambda_D}{2 \sin(\theta/2)}. \quad (69)$$

As discussed in Eq. (11), we need three stroboscopic lattices with the ratio of lattice constants

$$d_1 : d_2 : d_3 = \frac{1}{2} : \frac{\sqrt{3}}{4} : \frac{\sqrt{3}}{2}$$

to create the honeycomb lattice. This can be achieved by either adjusting the angle θ of the same laser light or choosing three laser lights with different wavelengths λ_D .

Interaction

At the low temperature in ultracold atom experiments, the collision of cold atoms is dominated by s -wave scattering process. The two-body interactions of ultracold gases in 3D can be described by a pseudopotential in the form of contact function [32]

$$V_{3D}(\mathbf{r}) = \frac{4\pi\hbar^2 a}{2m} \delta(\mathbf{r}), \quad (70)$$

where a is the s -wave scattering length. The scattering length a can be further tuned by the Feshbach resonance with a magnetic field B , i.e.,

$$a(B) = a_{bg} \left[1 - \frac{\Delta B}{B - B_0} \right]. \quad (71)$$

Here, a_{bg} is the off-resonant background scattering length, while ΔB and B_0 describe the width and position of the resonance.

In the quasi-1D trap, the strength of contact interaction can be modified by the transverse mode. The effective pseudopotential is described by an interaction of the form [32]

$$V_{1D}(x) = \frac{2\hbar\omega_{tr}a}{1 - Aa/l_{tr}} \delta(x) \approx 2\hbar\omega_{tr}a \delta(x), \quad (72)$$

where the constant $A = 1.036$ and $l_{tr} = \sqrt{\hbar/m\omega_{tr}}$ is the characteristic length of transverse motion. The approximation comes from the fact that the scattering length a is usually much shorter than the trapping length l_{tr} .

System size

During the collision, the kinetic energy of two atoms should not excite the transverse mode. This sets a restriction for the size (radius R) of phase space crystal, i.e.,

$$2 \times \frac{1}{2} m \omega_{ax}^2 \left(\frac{d}{2\pi} R \right)^2 < \hbar \omega_{tr} \quad \implies \quad R < \frac{2\pi}{d} \sqrt{\frac{\hbar \omega_{tr}}{m \omega_{ax}^2}} = \frac{2\pi}{d} \sqrt{\frac{\hbar \pi w_0}{m \lambda_L \omega_{ax}}}. \quad (73)$$

Quantum fluctuations

In the quantum regime, the atom localised in one lattice site may tunnel to another lattice site by quantum fluctuations due to $[X, P] = i\lambda$. We estimate the tunnelling rate between nearest-neighbor sites, which is the dominate tunnelling path as shown in Fig. 7(a). We expand the Hamiltonian along the dominant tunnelling path by

$$H \approx \frac{P^2}{2m(X)} + V(X), \quad (74)$$

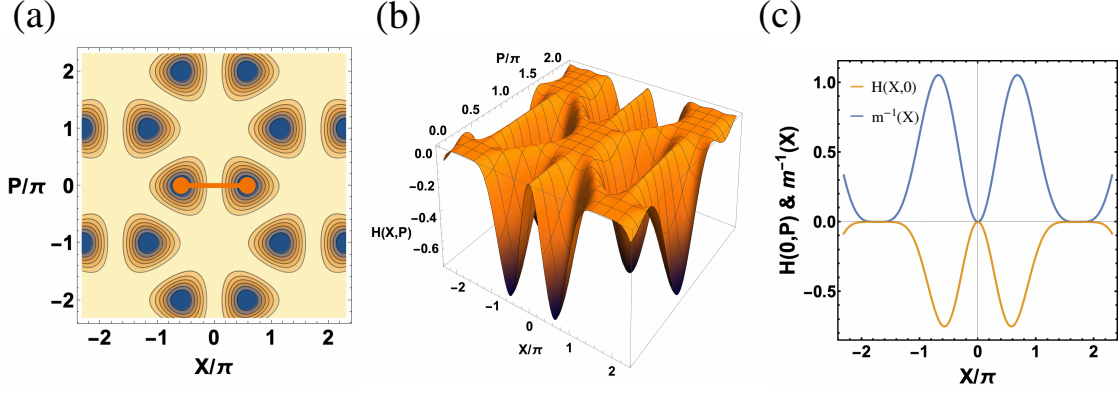


FIG. 7. (a) Density plot of phase-space honeycomb lattice Hamiltonian with orange line indicating the dominant tunnelling path. (b) 3D plot of phase-space honeycomb lattice Hamiltonian showing a double-well structure along the line $P = 0$. (c) The zero momentum cut of Hamiltonian $H(X, 0)$ (orange) and the inverse of effective mass $m(X)$ (blue).

where $V(X) = H_s(X, 0)$ has the form of double-well potential, and

$$m(X) = \left[\frac{\partial^2 H(X, P)}{\partial P^2} \right]^{-1} \quad (75)$$

plays the role of effective mass. For a given energy level E , the tunnelling rate can be calculated from the WKB approximation [13]

$$J = \frac{\lambda \omega_0}{2\pi} \exp \left(- \frac{1}{\lambda} \int_{-X_a}^{X_a} \left| \sqrt{2m(X)[E - V(X)]} \right| dX \right), \quad (76)$$

where $\pm X_a$ is the turning point given by $V(X_a) = E$. In our case, the integral of action is divergent resulting a zero tunnelling rate. In fact, since the 2nd derivative $\partial^2 H(X, P)/\partial P^2$ vanishes at this point at the saddle point of $V(X)$ Fig. 7(b), the effective mass is divergent at saddle point. In Fig. 7(c), we plot $V(X)$ and the inverse of mass $1/m(X)$ along the dominant tunnelling path.

Estimation of parameters

The parameters used for Figs. 3(c)-(g) in the main text could be obtained in an experiment with ultracold ^{87}Rb atoms. An appropriate experimental setup involves 8 lasers (4 for the static trapping, 2 for the stroboscopic trapping and 2 for the optomechanical detection), see sketch by Fig. 1(a) in the main text. Assuming a realistic longitudinal trapping frequency $\omega_{ax} = 2\pi \times 50 \text{ Hz}$ and $\omega_0 = 0.1$ (to guarantee slow vibrations in the rotating frame), the wavepacket's time of flight during a round-trip along the disk edge would be approximately $2\pi \times 50 / (\omega_{ax} \omega_0) \approx 10 \text{ s}$, shorter than the typical lifetime of the atom cloud [57–59]. With $k^{-1} = 45 \mu\text{m}$, one works in the semi-classical regime ($\lambda = 0.04$). In the experiment, the transverse trapping frequency can reach up to $\omega_{tr} \approx 2\pi \times 1.0 \text{ MHz}$ [32]. To avoid exciting the transverse mode during collisions, there is a restriction for the radius of the phase space crystal, cf. Eq. (73), $R < k \sqrt{\frac{\hbar \omega_{tr}}{m \omega_{ax}^2}} \approx 9.2\pi$. Taking into account the 3D scattering length $a = 5.3 \text{ nm}$ for ^{87}Rb atoms, the 1D dimensionless interaction strength is $\gamma = 2\hbar \omega_{tr} a k^3 / (m \omega_{ax}^2) \approx 1.25$, which can be further tuned by Feshbach resonance, cf. Eq. (71), or adjusting k .